

1 **High atmospheric oxidation capacity drives wintertime nitrate pollution in the eastern**
2 **Yangtze River Delta of China**

3

4 Han Zang¹, Yue Zhao^{1,*}, Juntao Huo², Qianbiao Zhao², Qingyan Fu², Yusen Duan^{2,*}, Jingyuan Shao³,
5 Cheng Huang⁴, Jingyu An⁴, Likun Xue⁵, Ziyue Li¹, Chenxi Li¹, Huayun Xiao¹

6

7 ¹School of Environmental Science and Engineering, Shanghai Jiao Tong University, Shanghai, 200240,
8 China

9 ²Shanghai Environmental Monitoring Center, Shanghai 200235, China

10 ³College of Flight Technology, Civil Aviation University of China, Tianjin 300300, China

11 ⁴Shanghai Academy of Environmental Sciences, Shanghai 200233, China

12 ⁵Environment Research Institute, Shandong University, Qingdao, Shandong, 266237, China

13

14 *Correspondence: Yue Zhao (yuezhao20@sjtu.edu.cn); Yusen Duan (duanys@yeah.net)

15

16 **Abstract**

17 Nitrate aerosol plays an increasingly important role in wintertime haze pollution in China. Despite
18 intensive research on the wintertime nitrate chemistry in recent years, quantitative constraints on
19 the formation mechanisms of nitrate aerosol in the Yangtze River Delta (YRD), one of the most
20 developed and densely populated regions in eastern China, remain inadequate. In this study, we
21 identify the major nitrate formation pathways and their key controlling factors during the winter
22 haze pollution period in the eastern YRD using two-year (2018-2019) field observations and
23 detailed observation-constrained model simulations. We find that the high atmospheric oxidation
24 capacity, coupled with high aerosol liquid water content (ALWC), made both the heterogeneous
25 hydrolysis of dinitrogen pentoxide (N_2O_5) and the gas-phase OH oxidation of nitrogen dioxide (NO_2)
26 important pathways for wintertime nitrate formation in this region, with contribution percentages of
27 69% and 29% in urban areas and 63% and 35% in suburban areas during the haze pollution episodes,
28 respectively. We further find that the gas-to-particle partitioning of nitric acid (HNO_3) was very
29 efficient so that the rate-determining step in the overall formation process of nitrate aerosol was the
30 oxidation of NO_x to HNO_3 through both heterogeneous and gas-phase processes. The atmospheric
31 oxidation capacity (i.e., the availability of O_3 and OH radicals) was the key factor controlling the
32 production rate of HNO_3 from both processes. During the COVID-19 lockdown (January-February
33 2020), the enhanced atmospheric oxidation capacity greatly promoted the oxidation of NO_x to
34 nitrate and hence weakened the response of nitrate aerosol to the emission reductions in urban areas.
35 Our study sheds light on the detailed formation mechanisms of wintertime nitrate aerosol in the
36 eastern YRD and highlights the demand for the synergetic regulation of atmospheric oxidation
37 capacity and NO_x emissions to mitigate wintertime nitrate and haze pollution in eastern China.

38

39 1. Introduction

40 Atmospheric fine particulate matter (PM_{2.5}) has profound impacts on air quality, climate, and public
41 health (Huang et al., 2014; Wang et al., 2014; Lelieveld et al., 2015; von Schneidmesser et al.,
42 2015). Over the past decades, China has encountered severe PM_{2.5} pollution due to the rapid
43 urbanization and industrialization (Huang et al., 2014; Zhang and Cao, 2015; Tao et al., 2017; Peng
44 et al., 2021). To tackle severe air pollution, Chinese government has implemented active clean air
45 policies such as the “Action Plan for Air Pollution Prevention and Control” in recent years. As a
46 result, anthropogenic emissions of major air pollutants such as sulfur dioxide (SO₂), nitrogen oxides
47 (NO_x), and primary PM have declined dramatically and the nationwide PM_{2.5} air quality have
48 improved significantly (Shao et al., 2018; Zheng et al., 2018; Ding et al., 2019; Zhang et al., 2019).
49 In addition, with the emission reduction of primary PM, secondary aerosol has become the most
50 important component of PM_{2.5} (Shao et al., 2018; Ding et al., 2019; Peng et al., 2021).

51

52 Secondary inorganic aerosol consisting mainly of nitrate, sulfate, and ammonium (SNA),
53 contributed to 30-60% of the PM_{2.5} mass in China (Hua et al., 2015; Tao et al., 2017; Ye et al., 2017;
54 Wang et al., 2018; Fu et al., 2020; Lin et al., 2020). During the pollution episodes, the proportion of
55 SNA to PM_{2.5} could exceed 50% (Tao et al., 2017; Liu et al., 2020a; Peng et al., 2021). Before 2013,
56 sulfate was often found to be the most abundant component of PM_{2.5} in Chinese cities (Zhao et al.,
57 2013; Huang et al., 2014; Kong et al., 2014; Xie et al., 2015; Tao et al., 2017). However, with the
58 implementation of stringent clean air policies, anthropogenic emissions of SO₂ in China had
59 dropped by 59% from 2013 to 2017, while NO_x emissions decreased only by 21% during the same
60 period (Zheng et al., 2018). Consequently, sulfate aerosol concentration has decreased dramatically
61 nationwide since 2013, but wintertime nitrate concentration has not decreased much (Ding et al.,
62 2019; Li et al., 2019a; Xu et al., 2019; Fu et al., 2020; Wang et al., 2020b); nitrate has become an
63 increasingly important component of PM_{2.5} in most regions of China during winter (Ye et al., 2017;
64 Yun et al., 2018; Li et al., 2019a; Xu et al., 2019; Chen et al., 2020; Fu et al., 2020; Kong et al.,
65 2020; Lin et al., 2020; Xie et al., 2020; Zhai et al., 2021; Zhang et al., 2021). The high loading of
66 nitrate has been considered playing an important role in winter haze pollution (Wen et al., 2015;
67 Sun et al., 2018). Therefore, identifying the major nitrate formation pathways and their controlling
68 factors during haze events is of great importance for developing effective particulate pollution
69 mitigation policies in China.

70

71 In polluted regions, the nitrate aerosol arises mainly from two pathways: (1) the gas-phase oxidation
72 of nitrogen dioxide (NO₂) by OH radicals producing nitric acid (HNO₃) (Calvert and Stockwell,
73 1983) and (2) the heterogeneous hydrolysis of dinitrogen pentoxide (N₂O₅) that was produced from
74 the reaction of NO₂ with nitrate (NO₃) radicals, on aqueous aerosols (Bertram and Thornton, 2009;
75 Bertram et al., 2009; Wagner et al., 2013; McDuffie et al., 2019). The gas-phase OH + NO₂ pathway
76 primarily occurs during the daytime and is mainly influenced by the atmospheric oxidation capacity
77 despite the NO₂ concentration (Chen et al., 2020; Fu et al., 2020). The heterogeneous formation of
78 nitrate via N₂O₅ hydrolysis is greatly affected by aerosol liquid water content (ALWC) and the

79 production of N_2O_5 (Alexander et al., 2020; Lin et al., 2020; Wang et al., 2020b). As a result, this
80 heterogeneous pathway is generally weak during the daytime because of the fast photolysis of NO_3
81 radicals and titration by NO (Wayne et al., 1991; Brown and Stutz, 2012), which inhibit N_2O_5
82 production. However, it could be the dominant pathway for nitrate formation during the nighttime
83 (Wang et al., 2017; McDuffie et al., 2019), where N_2O_5 can be produced more efficiently and its
84 hydrolysis is favored by the high relative humidity (or ALWC).

85
86 There have been a number of field studies on the pollution characteristics and formation
87 mechanisms of nitrate aerosol during haze events in China over the past decades (Tao et al., 2016;
88 Li et al., 2018; Sun et al., 2018; Wen et al., 2018; Ding et al., 2019; Ye et al., 2019; Chen et al., 2020;
89 Fu et al., 2020; Lin et al., 2020; Wang et al., 2020b; Zhao et al., 2020a; Chan et al., 2021). However,
90 most of these studies were carried out in the North China Plain (NCP) (Li et al., 2018; Wen et al.,
91 2018; Chen et al., 2020; Fu et al., 2020; Wang et al., 2020b; Chan et al., 2021). Earlier studies
92 suggested that the nitrate formation during the pollution episodes in this region was mainly
93 attributed to the heterogeneous hydrolysis of N_2O_5 (Su et al., 2017; Wang et al., 2017; He et al.,
94 2018; Li et al., 2018). However, recent studies showed that the gas-phase $\text{OH} + \text{NO}_2$ process has
95 become more important, and sometimes this process was even the dominant pathway for nitrate
96 formation (Chen et al., 2020; Fu et al., 2020). The Yangtze River Delta (YRD) in eastern China is
97 one of the most developed regions in China (Ding et al., 2013). The wintertime O_3 concentration is
98 relatively high in this region, with an average of ~ 20 ppb, and sometimes could even reach 75 ppb
99 (Li et al., 2019c; Ye et al., 2019; Zhao et al., 2020a), which is significantly higher than that (average:
100 6-16 ppb) in the NCP region (Li et al., 2019a; Duan et al., 2020; Liu et al., 2020a). Furthermore, the
101 relative humidity (RH) in this region is also high, with the average winter RH ranging from 63% to
102 71% (Tao et al., 2016; Shen et al., 2020; Yu et al., 2020b), which was also significantly higher than
103 the average RH (20-40%) in the NCP region (Fang et al., 2019; Li et al., 2019a; Huang et al., 2020;
104 Xie et al., 2020). The high atmospheric oxidation capacity, coupled with the high RH that led to
105 high ALWC, would favor the production of secondary aerosol (Peng et al., 2021).

106
107 Haze pollution events frequently occurred in the YRD during winter (Hua et al., 2015; Sun et al.,
108 2018; Ding et al., 2019). Although there have been many studies on the pollution characteristics of
109 nitrate and $\text{PM}_{2.5}$ in this region (Tao et al., 2016; Sun et al., 2018; Chen et al., 2019; Ding et al.,
110 2019; Ye et al., 2019; Lin et al., 2020; Shen et al., 2020), only a few studies have focused on the
111 nitrate formation mechanisms. It has been reported that the heterogeneous hydrolysis of N_2O_5
112 contributed dominantly to nitrate formation in the western YRD (Sun et al., 2018), and its
113 production rate could be 5 times higher than that of the gas-phase $\text{OH} + \text{NO}_2$ process during severe
114 haze pollution events (Lin et al., 2020). In contrast, some other studies have qualitatively pointed
115 out that the gas-phase $\text{OH} + \text{NO}_2$ reaction was an important formation pathway of nitrate in the
116 eastern YRD, though the heterogeneous hydrolysis of N_2O_5 during the nighttime also contributed
117 (Ye et al., 2019; Zhao et al., 2020a). Overall, quantitative constraints on the detailed formation
118 mechanisms of wintertime nitrate aerosol in the YRD region remain limited. The relative

119 contribution of different nitrate formation pathways and their controlling factors are still unclear.

120

121 In this study, we conducted hourly measurements of nitrate and associated particulate and gaseous
122 air pollutants at an urban site and a regional site in the eastern YRD during winter in 2018 and 2019,
123 aiming to clarify the nitrate formation mechanisms during winter. An observation-constrained box
124 model using the detailed Master Chemical Mechanism (MCM v3.3.1) updated with the state-of-the-
125 art heterogeneous chemistry of N_2O_5 , NO_2 , and particulate nitrate was employed to quantitatively
126 identify the major reaction pathways and key controlling factors for wintertime nitrate aerosol
127 formation in this region. This study will help to understand the nitrate aerosol chemistry in the
128 eastern YRD and develop effective strategies to mitigate secondary aerosol pollution in this densely
129 populated region.

130

131 **2. Materials and methods**

132 **2.1 Observation sites and instrumentation**

133 $\text{PM}_{2.5}$ and its chemical composition, inorganic gases, volatile organic compounds (VOCs), and
134 meteorological parameters were continuously measured at a regional site (Qingpu) and an urban site
135 (Pudong) in Shanghai from December 1 to February 12 in both 2018 and 2019. The Qingpu site
136 (120.989°E , 31.097°W) is a suburban site (see Fig. 1), located near the Dianshan Lake and
137 surrounded by the residential areas and vegetation, and about 46 km away from the urban Shanghai.
138 Besides, the Qingpu site is located at the junction of Shanghai, Jiangsu, and Zhejiang province and
139 is a typical regional site in the eastern YRD. The instruments at this site were on the rooftop of a 10
140 m tall building. The Pudong site (121.533°E , 31.228°W) is an urban site located near the Century
141 Avenue with heavy traffic, and it is only ~3 km from the business center Lujiazui. The instruments
142 at this site were located on the roof of a 20 m tall building. The eastern YRD region is affected by
143 the subtropical monsoon climate, dominated by the northwest and northeast winds in winter.

144

145 The measurements at the two sites were conducted hourly. The $\text{PM}_{2.5}$ mass concentration was
146 measured by a Tapered Element Oscillating Microbalance combined with Filter Dynamic
147 Measurement System (TEOM-FDMS, TEOM 1405-F, Thermo Fisher Scientific, USA.). Water-
148 soluble ions including NO_3^- , SO_4^{2-} , NH_4^+ , Cl^- , Na^+ , Ca^{2+} , and Mg^{2+} were measured using an online
149 Monitor for Aerosol and Gases (MARGA, ADI 2080, Applikon Analytical B.B.Corp., Netherlands).
150 Organic carbon (OC) and elemental carbon (EC) were measured by a semi-continuous OC/EC
151 analyzer (Model 4, Sunset Laboratory Inc., USA), and a denuder was installed before analyzer to
152 avoid the disturbance of organic vapors. The surface area and volume concentrations of aerosol
153 particles were measured using a scanning mobility particle sizer (SMPS, TSI, USA, which consists
154 of a 3080 electrostatic classifier, a 3081A differential mobility analyzer, and a 3787 condensation
155 particle counter) and an aerodynamic particle sizer (APS 3321, TSI, USA). The combination of
156 SMPS and APS was able to cover the particle size range from 13.6 nm to 10 μm . Considering that
157 the Pudong sampling site lacks the data of aerosol volume and surface area concentrations, we
158 performed a linear fit between the aerosol surface/volume and $\text{PM}_{2.5}$ mass concentration at the

159 Qingpu site (see Figure S1 in the supplement), and predicted the values for the Pudong site based
160 on such a linear fit and the measured PM_{2.5} mass concentration. The surface/volume concentrations
161 of dry aerosol particles measured by SMPS and APS were corrected to the ambient RH based on an
162 empirical composition-kappa function and the kappa-Köhler function (see details in Section S1 of
163 the Supplement). The O₃, NO_x, and SO₂ were measured by an Ozone, NO_x, and SO₂ analyzer (Model
164 49i, 42i, and 43i, Thermo Fisher Scientific, USA), respectively. A total of 56 VOCs were measured
165 using gas chromatography equipped with a flame ionization detector (GC-FID, Chromatotec
166 A11000/A21022 at the Qingpu site and PerkinElmer Clarus 580 at the Pudong site). Meteorological
167 parameters including temperature, RH, pressure, wind speed and direction were measured by a
168 meteorological transducer (WXT520, Vaisala Ltd., Finland).

169

170 **2.2 Estimation of aerosol liquid water content and pH**

171 The ISORROPIA-II thermodynamic model was used to calculate aerosol pH and ALWC
172 (Fountoukis and Nenes, 2007). The water-soluble inorganic ion concentrations, along with RH and
173 temperature, were used as the model input. The model was run in the forward mode, which would
174 give a more accurate estimation of aerosol pH than using the reverse mode with only particulate
175 inorganic ions as the model input (Guo et al., 2015; Hennigan et al., 2015). Besides, considering the
176 relatively high RH in eastern YRD, we selected the metastable state for aerosol in this study.
177 ISORROPIA-II calculated the equilibrium concentrations of particle hydronium ions (H_{air}⁺, μg m⁻³)
178 and ALWC (μg m⁻³) in per air volume. Then the aerosol pH can be derived by the following equation:

$$179 \quad \text{pH} = -\log_{10}(\text{H}_{\text{aq}}^+) = -\log_{10} \frac{1000\text{H}_{\text{air}}^+}{\text{ALWC}} \quad (1)$$

180 Where H_{aq}⁺ is the concentration of hydronium ions in aqueous aerosol (mol L⁻¹). It should be
181 mentioned that when the RH was extremely high (> 95%), a slight deviation in measured RH would
182 cause significant uncertainty in the estimation of ALWC. Therefore, we only considered the data
183 with the RH below 95% in the further analysis.

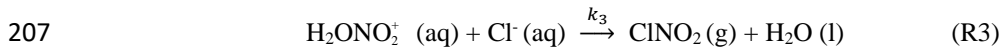
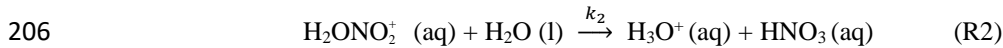
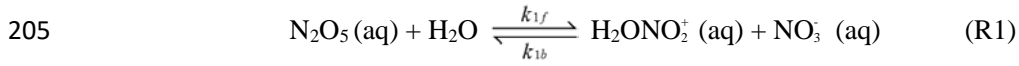
184

185 **2.3 Observation-constrained model simulation**

186 The Framework for 0-D Atmospheric Modeling (FOAM v3.1) (Wolfe et al., 2016) employing the
187 MCM v3.3.1 (Jenkin et al., 2015) was used to simulate the formation of nitrate in the pollution
188 events during the whole observation period. Figure 2 summarizes the formation pathways of HNO₃
189 in the atmosphere (Alexander et al., 2020; Chan et al., 2021). In the model, we considered the
190 reaction pathways including heterogeneous hydrolysis of N₂O₅ (R3) and NO₂ (R8), gas-phase OH
191 + NO₂ (R7), NO₃ radical oxidation of VOCs (R5), and reaction of NO with hydroperoxy (HO₂)
192 radicals (R2), which together contributed to 88% of HNO₃ formation in the global troposphere
193 (Alexander et al., 2020). The model did not include the hydrolysis of NO₃ radicals and organic
194 nitrate (R1, R4, and R6), as well as the reaction of NO₂ with halogen oxide species (R9). However,
195 these pathways only had a small contribution to the production of HNO₃ (Alexander et al., 2020).
196 Therefore, they would not significantly affect the model results in this study.

197

198 The default MCMv3.3.1 does not consider the heterogeneous hydrolysis of N₂O₅ in detail and the
 199 heterogeneous production of nitrous acid (HONO), an important precursor of OH radicals in the
 200 polluted atmosphere. Therefore, we parameterized these processes in the model based on recent
 201 advances in these processes. For the heterogeneous hydrolysis of N₂O₅, the N₂O₅ molecules
 202 accommodated on aqueous aerosols can undergo reversible hydrolysis to form NO₃⁻ and H₂ONO₂⁺
 203 (R1), followed by the reaction of H₂ONO₂⁺ with H₂O or Cl⁻ to form HNO₃ or nitryl chloride (ClNO₂)
 204 (R2 and R3) (Finlayson-Pitts et al., 1989; Schweitzer et al., 1998; Thornton and Abbatt, 2005):



208

209 The rate of the heterogeneous hydrolysis of N₂O₅ on aqueous aerosols (k_4) could be calculated by
 210 eq. 2 when ignoring the gas-phase diffusion limitation:

$$211 \quad k_4 = \frac{\gamma \text{N}_2\text{O}_5 \cdot c \cdot S_a}{4} \quad (2)$$

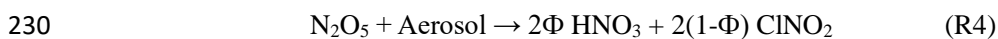
212 where $\gamma\text{N}_2\text{O}_5$ is the uptake coefficient of N₂O₅, defined as the probability of removal of N₂O₅ per
 213 collision with the wet aerosol surface; c is the mean molecular speed of N₂O₅; S_a is the measured
 214 aerosol surface area concentration. In this study, we employed an observation-based empirical
 215 parameterization of $\gamma\text{N}_2\text{O}_5$, which provided a reasonable representation of the PM_{2.5} reactivity
 216 toward N₂O₅ at different Chinese sites, according to a recent study (Yu et al., 2020a):

$$217 \quad \gamma\text{N}_2\text{O}_5 = \frac{4}{c} \frac{V_a}{S_a} K_H \times k_{1f} \times \left(1 - \frac{1}{\left(\frac{k_2}{k_{1b}} \times \frac{[\text{H}_2\text{O}]}{[\text{NO}_3^-]} \right) + 1 + \left(\frac{k_3}{k_{1b}} \times \frac{[\text{Cl}^-]}{[\text{NO}_3^-]} \right)} \right) \quad (3)$$

218 where V_a is the measured aerosol volume concentration; K_H is the Henry's law coefficient of N₂O₅,
 219 with a value of 51 M atm⁻¹ (Bertram and Thornton, 2009); k_{1f} is the second-order reaction rate
 220 constant of N₂O₅ with water, which was calculated using a linear function with [H₂O], as 3.0×10^4
 221 \times [H₂O] (Yu et al., 2020a); $\frac{k_2}{k_{1b}}$ and $\frac{k_3}{k_{1b}}$ are the relative rates of reactions of H₂ONO₂⁺(aq) with H₂O
 222 or Cl⁻ (R2 and R3) versus that with NO₃⁻ (the reverse reaction of R1), with values determined to be
 223 0.033 and 3.4, respectively (Yu et al., 2020a); and [H₂O], [NO₃⁻], and [Cl⁻] are the molarity of water,
 224 nitrate, and chloride in aerosol, respectively.

225

226 The yields (Φ , ranging between 0 and 1) of HNO₃ and ClNO₂ from the heterogeneous hydrolysis of
 227 N₂O₅ depend on the H₂O and Cl⁻ content in the aerosol (Bertram and Thornton, 2009; Yu et al.,
 228 2020a). In this study, the yield of HNO₃ (Φ_{HNO_3}) was estimated from eq. 4 (Bertram and Thornton,
 229 2009; Yu et al., 2020a):



231
$$\Phi_{HNO_3} = 1 - 1 / \left(1 + \frac{[H_2O]}{\frac{k_3}{k_2} \times [Cl^-]} \right) \quad (4)$$

232 where $\frac{k_3}{k_2}$ is the ratio of reaction rates of R3 versus R2, which has been determined to be 105 (Bertram
233 and Thornton, 2009; Yu et al., 2020a).

234
235 Photolysis of HONO was shown to contribute 20-92% of the production of OH radicals during
236 winter haze pollution events in China (Tan et al., 2017; Slater et al., 2020; Xue et al., 2020). Here,
237 on the basis of previous studies (Lee and Schwartz, 1983; Kleffmann et al., 1998; Kurtenbach et al.,
238 2001; Wong et al., 2011; Wong et al., 2013; Han et al., 2016; Ye et al., 2016; Liu et al., 2017; Trinh
239 et al., 2017; Romer et al., 2018; Zare et al., 2018; Liu et al., 2019; Wang et al., 2020a; Xue et al.,
240 2020), we parameterized the major heterogeneous production pathways of HONO and its dry
241 deposition to estimate the HONO budget during the pollution episodes. The added mechanisms are
242 summarized in Table 1. A detailed description of the parameterization is provided in the Supplement
243 (Section S2). Considering that there remain significant uncertainties in the key parameters (i.e., the
244 uptake coefficient of NO₂ on aerosol or ground surfaces, EF, and HONO emission ratios) of the
245 heterogeneous HONO formation pathways and its direct emissions as listed in Table 1, we
246 performed the sensitivity analyses for these parameters to evaluate their influences on the model
247 results.

248
249 In addition, we considered the dilution of species via deposition, entrainment, etc. using a highly
250 simplified parameterization:

251
$$\frac{d[X]}{dt} = -k_{dil} ([X] - [X]_{bkg}) \quad (5)$$

252 where k_{dil} is the first-order dilution rate constant; $[X]_{bkg}$ is a fixed background concentration of
253 pollutants. Here, a typical dilution lifetime of one day was assumed, i.e., $k_{dil} = 1/24 \text{ h}^{-1}$. As the
254 species background concentration was unknown, $[X]_{bkg}$ was set to 0 for simplicity. Considering the
255 uncertainties in the parameterization of dilution process using a constant rate constant, we also
256 conducted a sensitivity test for k_{dil} with its value ranging between 0.028 h^{-1} and 0.2 h^{-1} , which covers
257 the typical values used in box model simulations (Romer et al., 2018; McDuffie et al., 2019; Liu et al.,
258 2020b), to evaluate its influence on the model results.

259
260 In the model, the j values of various gaseous species were calculated using the default MCMv3.3.1
261 parameterization with input of the solar zenith angle at the observations sites and scaled by the ratio
262 of measured to calculated jNO_2 values. The observed pollutant concentrations and meteorological
263 parameters were used as the model input, which were updated hourly (one model step) using the
264 observation data and held constant during each model step, except for the observed concentrations
265 of NO and NO₂ (the sum of NO and NO₂ concentrations was constrained by the observation, but
266 their specific ratios were simulated by the model).

267

268 3. Results and Discussion

269 3.1 Overview of pollution characteristics during winter

270 Table 2 shows the overall pollution conditions of the two observation sites in winter 2018 and 2019.
271 The average $PM_{2.5}$ concentration increased by 17-21% in 2019 compared to that in 2018.
272 Accordingly, nitrate concentration also increased by 11-14% in 2019. The O_3 concentration was
273 slightly higher in 2019 than in 2018, consistent with increased atmospheric oxidation capacity in
274 recent years (Lu et al., 2018; Li et al., 2019b; Liu and Wang, 2020; Yang et al., 2020). In the two
275 years, both of the $PM_{2.5}$ and nitrate concentrations at the Qingpu site were higher than those at the
276 Pudong site. As mentioned above, the Qingpu site is at the junction of Shanghai, Jiangsu, and
277 Zhejiang, so it is more easily influenced by the transport of air pollutants from Jiangsu, which is
278 usually more polluted than Shanghai. Besides, the average temperature at the Qingpu site was also
279 slightly lower than that at the Pudong site, which might to some extent favor the gas-to-particle
280 partitioning of HNO_3 . Notably, the average RH was as high as 80% during the observation period,
281 which was significantly higher than that (63%) recorded in 2016 (Tao et al., 2016). In particular, the
282 RH exceeded 90% for more than one third of the days during the observation period.

283

284 Taking the Pudong site in 2019 as an example, we analyzed the time series of $PM_{2.5}$, nitrate, and
285 other related parameters and presented the results in Figure 3 (Time series of the pollutants at the
286 Qingpu site can be seen in Section S3 and Figure S2). $PM_{2.5}$ pollution events occurred frequently in
287 the eastern YRD during winter. During the observation period, the $PM_{2.5}$ concentration exceeded 75
288 $\mu g m^{-3}$ for 34 days and $150 \mu g m^{-3}$ for 6 days. During the pollution episodes ($PM_{2.5} > 75 \mu g m^{-3}$),
289 nitrate had become the most important component of $PM_{2.5}$, and its concentration was a factor of
290 2.2 higher than that of sulfate. In winter, the emission of NO_x was obviously high. During the periods
291 with high nitrate concentration, the NO_x concentration always exceeded 100 ppb. The O_3
292 concentration was also at a relatively high level, with a maximum value of 60 ppb and an average
293 of 22 ppb, which was much higher than the wintertime average O_3 concentration (6-16 ppb) in the
294 NCP (Li et al., 2019a; Duan et al., 2020; Liu et al., 2020a). The concentration of odd oxygen
295 ($O_x = O_3 + NO_2$) ranged between 20-83 ppb with an average of 44 ppb, indicating a relatively high
296 atmospheric oxidation capacity in the eastern YRD during winter. Consistently, the nitrogen
297 oxidation ratio (NOR, $NOR = NO_3 / (NO_3 + NO_2)$) was up to 0.51, suggesting a high degree of
298 atmospheric oxidation. Meanwhile, the high atmospheric RH in the eastern YRD led to a high
299 ALWC. During the high nitrate periods, the ALWC was often at its peak and could exceed $200 \mu g$
300 m^{-3} on rainy or haze-foggy days. Such a high ALWC level would have an important impact on the
301 nitrate formation. Notably, the NO_x concentration dropped sharply on 23 January and kept at a low
302 level until the end of the observation (12 February, 2020). This is mainly a result of marked emission
303 reductions during the COVID-19 lockdown. Such an emission reduction had a complicated
304 influence on the nitrate formation chemistry, which will be discussed in detail in Section 3.5.

305

306 Figure 4 shows the mass ratio of nitrate to $PM_{2.5}$ as a function of the $PM_{2.5}$ concentration and ALWC
307 at Qingpu and Pudong sites in 2018 and 2019. The ratio of nitrate to $PM_{2.5}$ increased with increasing

308 PM_{2.5} concentration. When the PM_{2.5} concentration was above 75 μg m⁻³, the average mass fraction
309 of nitrate was more than 30%. In addition, the nitrate formation rate was much higher than that of
310 sulfate and ammonium during PM_{2.5} pollution episodes, as indicated by the slope of nitrate vs. PM_{2.5}
311 that was twice that of the other two ions (see Figure S3). These results indicate that the formation
312 of nitrate played a driving role in the formation of PM_{2.5} pollution. In general, when the ALWC was
313 high, the nitrate concentration was also at a high level. On one hand, ALWC could promote the
314 nitrate formation by favoring the heterogeneous hydrolysis of N₂O₅ and the gas-to-particle
315 partitioning of HNO₃. On the other hand, the increase in nitrate concentration could enhance the
316 hygroscopicity of PM_{2.5}, leading to an increase in ALWC, which would further promote the nitrate
317 formation (Wang et al., 2020b). It is worth noting that, when PM_{2.5} < 100 μg m⁻³, the mass ratio of
318 NO₃⁻ to PM_{2.5} increased rapidly with rising PM_{2.5} concentration, but when the PM_{2.5} concentration
319 exceeded 100 μg m⁻³, the ratio reached a plateau. This might be due to the fact that when the PM_{2.5}
320 concentration increased to a certain level, the formation process of other components may also speed
321 up, causing the nitrate proportion to stay basically constant.

322

323 3.2 Gas-to-particle partitioning of nitrate

324 The gas-to-particle partitioning of nitrate determines the sensitivity of particulate nitrate formation
325 to the production of HNO₃. Figure 5 shows the particulate nitrate concentration (measured) and its
326 fraction to total nitrate (ϵHNO_3 , $\epsilon\text{HNO}_3 = \text{NO}_3^- / (\text{NO}_3^- + \text{HNO}_3)$), predicted by ISORROPIA-II) as a
327 function of ALWC and aerosol pH. In order to avoid the influence of rainy and foggy days during
328 the observation period which could lead to the abnormal high ALWC, we only used the data with
329 RH below 95% for analysis. Obviously, ALWC promoted the formation of particulate nitrate, but
330 such a promoting effect varied greatly under different aerosol pH (top panel in Figures 5a-d). As the
331 pH increased, the slope of nitrate vs. ALWC also increased significantly, indicating a stronger
332 promoting effect. ALWC plays a dual role in the formation of nitrate aerosol: it can promote the
333 heterogeneous formation of nitrate, e.g., via N₂O₅ hydrolysis, by providing more reaction medium
334 and decreasing the kinetic limitation (Mozurkewich and Calvert, 1988; Bertram and Thornton, 2009;
335 Wang et al., 2020b); the ALWC can also promote the gas-to-particle partitioning of HNO₃. The
336 different promoting effect of ALWC under different aerosol pH is mainly due to the fact that pH can
337 significantly influence the gas-to-particle partitioning of HNO₃. As shown in Figures 5a-d (bottom
338 panel), when the aerosol pH was low, the gas-to-particle partitioning of HNO₃ was inhibited, with
339 the value of ϵHNO_3 basically below 0.6 at pH < 2. Under these conditions, the increase of particulate
340 nitrate concentration would require more ALWC. When the pH increased, the inhibition effect of
341 pH on the gas-to-particle partitioning of HNO₃ was weakened. When the pH was higher than 2.5,
342 the nitrate was almost in the particle phase ($\epsilon\text{HNO}_3=1$). As a result, the increase of ALWC would
343 rapidly promote the nitrate formation, particularly when ALWC was at a low level. It is important
344 to point out that during the whole observation period, the values of ϵHNO_3 were larger than 0.9 for
345 90% of time when the PM_{2.5} concentration was higher than 75 μg m⁻³ (see Figure S4). This indicates
346 that the gas-to-particle partitioning of HNO₃ was very efficient and not a limiting factor for
347 particulate nitrate formation during the pollution episodes. The gas-to-particle partitioning of HNO₃

348 was also efficient in the NCP region, and its average ϵHNO_3 could reach 100% during the haze
349 pollution period (Guo et al., 2018; Li et al., 2019a). However, the average ϵHNO_3 in the northeastern
350 United States during winter was only 39% (Guo et al., 2018), this might be due to the relatively
351 lower pH in this region (0.8 ± 1.0) (Guo et al., 2016), which inhibited the gas-to-particle partitioning.
352

353 **3.3 Observational constraints on the nitrate formation mechanism**

354 The dominant nitrate formation pathway is different during the different time of a day. The
355 heterogeneous hydrolysis of N_2O_5 was often found to be an important pathway for nighttime nitrate
356 formation. Here, we evaluated the role of this pathway to nitrate formation in the eastern YRD using
357 the nighttime averages correlation between particulate nitrate concentration and the production of
358 N_2O_5 . Due to the lack of direct observational data of N_2O_5 in this study, we used the value of square
359 of NO_2 multiplied by O_3 ($[\text{NO}_2]^2 \times \text{O}_3$) to indicate the N_2O_5 level (Liu et al., 2020a). Figure 6 shows
360 the nighttime average nitrate concentration as a function of $[\text{NO}_2]^2 \times \text{O}_3$ in winter. The average
361 particulate nitrate concentration showed a strong positive correlation with $[\text{NO}_2]^2 \times \text{O}_3$. In particular
362 in 2019, as the value of $[\text{NO}_2]^2 \times \text{O}_3$ increased to $\sim 15000 \text{ ppb}^3$, the nitrate concentration increased
363 from $15\text{-}20 \mu\text{g m}^{-3}$ to $40\text{-}45 \mu\text{g m}^{-3}$, suggesting that the heterogeneous hydrolysis of N_2O_5 was an
364 important pathway for wintertime nitrate formation in the eastern YRD. Notably, there are some
365 data points with low values of $[\text{NO}_2]^2 \times \text{O}_3$ but high nitrate concentrations. This might be partly due
366 to their relatively high aerosol pH (> 3), which could promote the gas-to-particle partitioning of
367 HNO_3 .

368

369 To evaluate the role of the gas-phase $\text{OH} + \text{NO}_2$ process in nitrate formation during the daytime, we
370 use the O_x to indicate the atmospheric oxidation capacity due to the lack of direct observational data
371 of OH radicals. Figure 7 shows the daytime average particulate nitrate concentration as a function
372 of O_x . Notably, as the O_x concentration increased, the nitrate concentration also increased
373 significantly. However, the increase in ALWC seemed to have a relatively small impact on the
374 nitrate concentration during the daytime, indicating that the reaction of NO_2 with OH radicals to
375 form HNO_3 (rather than the gas-to-particle partitioning) was a rate-limiting step in daytime nitrate
376 formation. We also note that there are some data points with low O_x values but high ALWC and
377 nitrate concentrations (Figure 7c). This phenomenon might be owing to a certain degree of
378 heterogeneous process in the haze-foggy days, when the photochemical reactions were relatively
379 weak. Overall, the high atmospheric oxidation capacity made the gas-phase $\text{OH} + \text{NO}_2$ reaction an
380 important pathway for nitrate formation during the daytime in the eastern YRD.

381

382 **3.4 Model constraints on the nitrate formation mechanism**

383 To quantify the contribution of different formation mechanisms to wintertime nitrate formation in
384 the eastern YRD, we used an observation-constrained model (F0AM v3.1) updated with the
385 heterogeneous chemistry of N_2O_5 and NO_2 (see Section 2.3 for details) to simulate the formation
386 rate of HNO_3 from different pathways during the observation period. During the winter of 2019, six
387 haze pollution episodes ($\text{PM}_{2.5} > 75 \mu\text{g m}^{-3}$) occurred at both sites (there was an additional episode

388 during the outbreak of COVID-19 epidemic, which was discussed separately in Section 3.5). We
389 conducted simulations for all the six pollution episodes and took two representative ones at the
390 Pudong site for the detailed analysis. Considering the large uncertainties in ALWC estimation and
391 aerosol surface area/volume correction at high RH levels ($> 95\%$), which could significantly affect
392 the simulation results, we excluded the simulated data above 95% RH from the further analysis.
393 Figure 8 shows the time series of various particulate (measured) and gaseous (measured and
394 simulated) air pollutants, as well as the formation rate of HNO_3 (simulated) from different pathways
395 during these two episodes (The case studies of the same episodes at the Qingpu site are given in
396 Section S4 and Figure S5).

397

398 In episode 1 (Figure 8a), the nitrate concentration increased rapidly from $15.2 \mu\text{g m}^{-3}$ at 22:00 on
399 29 December to $39.0 \mu\text{g m}^{-3}$ at 10:00 on 30 December, with an average growth rate of $2.0 \mu\text{g m}^{-3} \text{h}^{-1}$.
400 The simulated NO_2 concentration was in good agreement with the observation, except for a short
401 period around the midnight of 30 December, during which the NO emissions led to an over-
402 prediction of the NO_2 level. During the high nitrate periods, the nighttime N_2O_5 concentration could
403 reach 0.5-1 ppb and contributed noticeably to HNO_3 formation via the heterogeneous hydrolysis.
404 However, the high daytime OH concentration (up to 2.5×10^6 molecules cm^{-3}) facilitated a relatively
405 more rapid nitrate formation from the gas-phase $\text{OH} + \text{NO}_2$ pathway. The average production rate
406 of HNO_3 from the gas-phase $\text{OH} + \text{NO}_2$ reaction during the daytime was $2.9 \mu\text{g m}^{-3} \text{h}^{-1}$, which was
407 twice the average production rate of HNO_3 from the heterogeneous hydrolysis of N_2O_5 during the
408 nighttime.

409

410 We note that the overestimation of NO_2 during the night of 30 December (case 1) could lead to an
411 overestimation of nighttime HONO , but it did not significantly affect the overall production rate of
412 HONO and thereby OH radicals in this case, which was dominated by the daytime heterogeneous
413 photochemical processes (see Figure S7, HONO production rate in the base scenario). In addition,
414 as the O_3 concentration in the model was constrained by the measured value, which was very low
415 (< 5 ppb) during this time, the overestimation of NO_2 would also not significantly affect the
416 prediction of N_2O_5 . As a result, the over-prediction of NO_2 would not have a large influence on the
417 major formation pathways of nitrate.

418

419 There were two cases in the episode 2 (Figure 8b). In case 2, the concentration of nitrate increased
420 from $26.8 \mu\text{g m}^{-3}$ at 05:00 to $46.0 \mu\text{g m}^{-3}$ at 13:00 on 12 January, 2020, with an average growth rate
421 of $2.4 \mu\text{g m}^{-3} \text{h}^{-1}$. Then, the nitrate concentration achieved a fast growth from 40.2 to $70.5 \mu\text{g m}^{-3}$
422 within only six hours during the night of 12 January, with an average rate of $5.1 \mu\text{g m}^{-3} \text{h}^{-1}$. During
423 the nitrate increasing period, the maximum OH concentration was $\sim 1.0 \times 10^6$ molecules cm^{-3} . As a
424 result, the gas-phase $\text{OH} + \text{NO}_2$ reaction led to a slow increase of nitrate concentration in the daytime
425 of 12 January. During the nighttime, the N_2O_5 concentration quickly increased to 0.83 ppb. The high
426 N_2O_5 level, in combination with the high ALWC, made the heterogeneous hydrolysis of N_2O_5 a
427 more important pathway for nitrate formation. The simulated average production rate of HNO_3 from

428 the heterogeneous hydrolysis of N_2O_5 during this case was $4.0 \mu\text{g m}^{-3} \text{h}^{-1}$, which was 3.6 times that
429 of the formation rate from the gas-phase $\text{OH} + \text{NO}_2$ reaction ($1.1 \mu\text{g m}^{-3} \text{h}^{-1}$). In case 3, the nitrate
430 concentration increased from $22.5 \mu\text{g m}^{-3}$ at 0:00 to $53.8 \mu\text{g m}^{-3}$ at 11:00 on 14 January, with an
431 average growth rate of $2.8 \mu\text{g m}^{-3} \text{h}^{-1}$. The N_2O_5 concentration was at a high level (~ 1 ppb) during
432 the nighttime and its hydrolysis contributed significantly to nitrate formation at the beginning of the
433 nitrate-increasing period. In the morning of 14 January, the OH concentration rapidly increased to
434 1.3×10^6 molecules cm^{-3} , resulting in considerable nitrate formation from the gas-phase process.
435 The average production rates of HNO_3 from the heterogeneous and gas-phase processes in this case
436 were 3.9 and $2.4 \mu\text{g m}^{-3} \text{h}^{-1}$, respectively, suggesting that both processes were important nitrate
437 formation pathways.

438

439 As mentioned above, there were six haze pollution episodes during the observation period. At the
440 Qingpu site, the heterogeneous hydrolysis of N_2O_5 was the major formation pathway (65-80%) of
441 nitrate aerosol for four episodes, while the gas-phase $\text{OH} + \text{NO}_2$ reaction had a major contribution
442 (54-60%) for the other two episodes. At the Pudong site, the heterogeneous process also contributed
443 dominantly (67-89%) to nitrate formation during four episodes, and for the other two episodes, the
444 contributions of the heterogeneous and gas-phase processes were comparable (51-53% vs. 45-47%).
445 Figure S6 shows the average diurnal variation of the production rates of HNO_3 from different
446 pathways during the observation period in 2019. The gas-phase process produced HNO_3 mainly
447 from 7:00 to 16:00, while the HNO_3 production from the heterogeneous process occurred mainly
448 from 17:00 to 6:00. The average production rates of HNO_3 from the heterogeneous and gas-phase
449 processes are given in Figure 9. At the Qingpu site, the average production rate of HNO_3 from the
450 two processes was $3.79 \mu\text{g m}^{-3} \text{h}^{-1}$ for the heterogeneous process during the nighttime (14 hours) vs.
451 $2.94 \mu\text{g m}^{-3} \text{h}^{-1}$ for the gas-phase reaction during the daytime (10 hours). The production rate from
452 other processes such as NO_2 hydrolysis and NO_3 radical oxidation of VOCs was only $0.08 \mu\text{g m}^{-3}$
453 h^{-1} . Therefore, the heterogeneous and gas-phase processes contributed to 63% and 35% of nitrate
454 formation at this site, respectively. At the Pudong site, the average formation rate of HNO_3 from the
455 hydrolysis of N_2O_5 was $3.83 \mu\text{g m}^{-3} \text{h}^{-1}$, significantly higher than that from the gas-phase reaction
456 ($2.27 \mu\text{g m}^{-3} \text{h}^{-1}$). As a result, the contributions of heterogeneous and gas-phase processes to nitrate
457 formation were 69% and 29%, respectively.

458

459 As mentioned in Section 2.3, significant uncertainties remain in the key parameters of the
460 heterogeneous HONO formation pathways and the dilution process in the model, which could affect
461 the prediction of OH radicals and N_2O_5 and thereby the production of HNO_3 . However, sensitive
462 analyses for various parameters show that the current parameterization of the heterogeneous HONO
463 formation and dilution process in the model allows for robust quantitative constraints on the relative
464 contributions of the gas-phase and heterogeneous processes to nitrate formation during haze
465 pollution episodes (see Section S5 and Figures S7, S8 for more details). In addition, monoterpenes
466 that are very reactive to NO_3 radicals (Atkinson and Arey, 2003) were not included in the model,
467 because their measurements are not available in this study. However, a case study considering the

468 monoterpene chemistry in the model shows that the low monoterpene emissions during the winter
469 did not significantly affect the budget of NO₃ radical and N₂O₅ and thereby the nighttime HNO₃
470 production (see Section S6 and Figure S9 for more details).

471

472 As discussed in Section 3.2, the gas-to-particle partitioning of HNO₃ was rather efficient, with the
473 value of ϵ_{HNO_3} larger than 0.9 for 90% of the time during the haze pollution periods. Therefore,
474 the overall formation rate of particulate nitrate would be determined by the production rate of HNO₃
475 from the heterogeneous hydrolysis of N₂O₅ and gas-phase OH + NO₂ reaction. To identify the key
476 chemical factors that controlled the production rates of HNO₃ from these two major reaction
477 pathways, the relationships between the HNO₃ production rate and concentrations of NO₂ and
478 oxidants (i.e., O₃ or OH radicals) are examined and plotted in Figure 10.

479

480 As shown in Figure 10a, the slopes of the HNO₃ production rate from the heterogeneous process vs.
481 NO₂ during the nighttime were different under different O₃ concentrations. When O₃ concentrations
482 were higher than 10 ppb, the increase in NO₂ led to a significant increase in HNO₃ production, with
483 the production rate exceeding 5 $\mu\text{g m}^{-3} \text{h}^{-1}$ when the NO₂ was higher than 30 ppb. However, when
484 the O₃ level was low (< 10 ppb), the heterogeneous process was relatively slow, even with NO₂
485 concentration exceeding 60 ppb. These results suggest that the atmospheric oxidation capacity (or
486 the availability of O₃), which affected the production of N₂O₅, played a vital role in controlling the
487 nitrate formation rate from the heterogeneous process. Furthermore, the reactive uptake of N₂O₅ by
488 aerosols was found to be very efficient (see Figure S10) so that it was not the rate-limiting step of
489 the heterogeneous nitrate formation during the haze pollution periods. Similarly, the slope of the
490 HNO₃ production rate from the gas-phase process vs. NO₂ during the daytime also varied
491 dramatically under different OH radical concentrations (Figure 10b). As the OH radical
492 concentration was higher than 7×10^5 molecules cm⁻³, this rate increased markedly with the increase
493 in NO₂. This phenomenon proved again that the atmospheric oxidation capacity played a driving
494 role in the production of HNO₃ from the gas-phase process.

495

496 The results in Figure 10 also suggest that solely reducing the NO_x emissions might result in an
497 increase of O₃ and OH concentrations (Lu et al., 2019; Zhao et al., 2020b), which could enhance the
498 oxidation of NO_x and thereby offset the effect of NO_x emission reductions on HNO₃ production.
499 Therefore, a synergistic control of atmospheric oxidant and NO_x emissions would be of great
500 importance for mitigating wintertime particulate nitrate pollution in the eastern YRD.

501

502 **3.5 Nitrate aerosol formation during the COVID-19**

503 The city lockdowns during the COVID-19 epidemic resulted in substantial emission reductions from
504 vehicular and industrial sources, which provided an opportunity to investigate the response of
505 secondary aerosols to primary emission reductions. Here, we selected the 23 January, 2019 as a
506 demarcation point (since then many cities in China started to implement lockdown measures) and
507 analyzed the characteristics of particulate nitrate pollution before and during the COVID-19

508 epidemic.

509

510 Figure 11 shows the concentrations of major gaseous and particulate air pollutants, NOR, and sulfur
511 oxidation ratio (SOR) in the eastern YRD before (1-22 January, 2020) and during (23 January-12
512 February, 2020) the COVID-19 epidemic. At the Pudong site (Figure 11 a, b, c), the average NO_x
513 concentration decreased by 57% due to marked reductions in vehicular emissions during the
514 epidemic. In contrast, the SO_2 concentration only had a small decrease (16%) during the epidemic,
515 since it mainly comes from coal-combustion sources and is less affected by vehicular emissions.
516 However, the O_3 concentration increased by 66% during the epidemic. This is mainly due to the
517 significant reduction in NO_x emissions, though the changes in meteorological conditions could also
518 contribute (Zhao et al., 2020b). Accordingly, the model simulations show that the atmospheric OH
519 concentration (median) increased by 14% during the epidemic, though the average value only
520 increased slightly. The increase in O_3 and OH concentrations could significantly promote the
521 oxidation of NO_x to nitrate and SO_2 to sulfate through both gas-phase and heterogeneous processes.
522 As shown in Figure 11c, the average values of NOR and SOR increased from 0.15 and 0.46 before
523 the epidemic to 0.21 and 0.50 during the epidemic, respectively. The enhanced oxidation of NO_x
524 and SO_2 would weaken the response of particulate nitrate and sulfate to the emission reductions. As
525 can be seen in Figure 11b and c, the simulated HNO_3 production rate and measured particulate nitrate
526 concentration dropped by 42% and 40% during the epidemic, respectively, which were both
527 significantly smaller than the decrease in NO_x concentration (57%), while the particulate sulfate
528 concentration only decreased by 2%, also substantially smaller than the reduction in SO_2
529 concentration (16%).

530

531 Similarly, at the Qingpu site, the NO_x concentration decreased by 58% during the epidemic, while
532 the concentrations of O_3 and OH radicals (median) increased by 90% and 17%, respectively. The
533 significantly enhanced atmospheric oxidation capacity made the simulated HNO_3 production rate
534 only decrease by 17% during the epidemic. However, the measured particulate nitrate concentration
535 at this site decreased by 60%, comparable to the decrease in NO_x concentration. The inconsistency
536 between the decrease in measured nitrate concentration and simulated HNO_3 production rate at the
537 Qingpu site was different from the situation observed at the Pudong site, which is likely due to the
538 fact that the Qingpu site was more easily to be influenced by the regional transport. We note that the
539 average wind speed at the Qingpu site (1.8 m s^{-1}) was higher than that at the Pudong site (1.1 m s^{-1}).
540 Besides, the haze pollution was more serious at the Qingpu site than at the Pudong site before
541 the epidemic: both $\text{PM}_{2.5}$ and nitrate concentrations were significantly higher at the Qingpu site (see
542 Figure 11). Therefore, the marked emission reductions on a regional scale during the epidemic
543 would decrease both the local formation and transport of particulate nitrate from the upwind regions,
544 resulting in a more pronounced reduction in observed nitrate concentration at the Qingpu site. In
545 addition, before the epidemic, the transport of aged air plume with relatively high nitrate and sulfate
546 concentrations from upwind regions resulted in relatively high NOR and SOR values at the Qingpu
547 site. However, during the epidemic, the significant decrease in nitrate and sulfate concentrations in

548 the aged air plume due to regional emission reductions led to lower NOR and SOR at this site.

549

550 The results at the Pudong site clearly show that the enhanced atmospheric oxidation capacity during
551 the COVID-19 epidemic promoted the formation of secondary aerosols and offset the effects of
552 primary emission reductions in the eastern YRD. Such a phenomenon has also been observed in
553 many other regions in China during the COVID-19 lockdown (Le et al., 2020; Zheng et al., 2020;
554 Huang et al., 2021; Liu et al., 2021; Tian et al., 2021; Zhong et al., 2021). These results suggest an
555 important role of atmospheric oxidation capacity in regulating secondary aerosol formation. They
556 also highlight the importance of the synergetic regulation of atmospheric oxidants and other air
557 pollutants in the mitigation of particulate pollution in China. However, the Qingpu site also provided
558 us a special case that in severely polluted regions with a stronger influence from the regional
559 transport, the offset effects of enhanced atmospheric oxidation capacity on emission reductions
560 could be more complicated and less significant.

561

562 **4. Conclusions**

563 In this study, the chemical mechanisms and key controlling factors of wintertime nitrate formation
564 in the eastern YRD of China were investigated using a combination of online field observations and
565 detailed model simulations. During the observation period (Winter 2018 and 2019), the haze
566 pollution events ($PM_{2.5} > 75 \mu g m^{-3}$) occurred frequently in this region. The mass fraction of nitrate
567 in $PM_{2.5}$ increased dramatically with $PM_{2.5}$ concentration and exceeded 30% throughout the
568 pollution periods. The measured nitrate concentration was well correlated with $[NO_2]^2 \times [O_3]$ (an
569 indicator of N_2O_5) at night and the level of O_x (an indicator of atmospheric oxidation capacity)
570 during the daytime, indicating that both the heterogeneous hydrolysis of N_2O_5 and gas-phase $OH +$
571 NO_2 process played important roles in wintertime nitrate formation in the eastern YRD.
572 Observation-constrained model simulations further show that the average production rates of HNO_3
573 from the heterogeneous hydrolysis of N_2O_5 during the nighttime and gas-phase $OH + NO_2$ reaction
574 during the daytime were $3.81 \mu g m^{-3} h^{-1}$ and $2.61 \mu g m^{-3} h^{-1}$, respectively, during the haze pollution
575 periods; these two pathways accounted for 66% and 32% of wintertime nitrate formation in the
576 eastern YRD, respectively.

577

578 The ALWC significantly promoted the formation of nitrate by facilitating the hydrolysis of N_2O_5
579 and the gas-to-particle partitioning of HNO_3 . However, the promoting effect of ALWC on nitrate
580 formation varied with aerosol pH due to its significant influence on the gas-to-particle partitioning
581 of HNO_3 . During the pollution periods, the gas-to-particle partitioning of HNO_3 was very efficient,
582 with the partitioning coefficients, ϵ_{HNO_3} , larger than 0.9 for 90% of the time. Therefore, the overall
583 formation processes of wintertime particulate nitrate were not limited by the gas-to-particle
584 partitioning of HNO_3 but rather by its production from both heterogeneous and gas-phase processes.
585 Further analyses of the response of HNO_3 formation to the variation in the concentrations of NO_2 ,
586 O_3 , and OH radicals suggests that the atmospheric oxidation capacity (i.e., the availability of O_3 and
587 OH radicals) played a key role in controlling the formation of nitrate from both processes.

588 During the COVID-19 lockdown (January-February 2020), the enhanced atmospheric oxidation
589 capacity promoted the oxidation of NO_x to nitrate and weaken the effects of primary emission
590 reductions on particulate pollution in typical urban areas in the eastern YRD, though such an offset
591 effect was less significant in regions with a stronger influence from the regional transport. This
592 phenomenon again suggests that the atmospheric oxidation capacity played an important role in
593 driving the formation of secondary aerosols, and highlights the importance of the synergetic
594 regulation of atmospheric oxidation capacity and other air pollutants in the mitigation of particulate
595 pollution in eastern China.

596

597 *Data availability.* The data presented in this work are available upon request from the corresponding
598 authors.

599

600 *Author contributions.* YZ designed the study, JH, QZ, QF, and YD performed field measurements,
601 JYS conducted ISORROPIA-II model calculation, JA and CH provided the NO_x emission inventory,
602 and YZ and HZ analyzed the data, conducted model simulations, and wrote the paper. All other
603 authors contributed to discussion and writing.

604

605 *Competing interests.* The authors declare no conflict of interest.

606

607 *Acknowledgments.* Yue Zhao acknowledges the Program for Professor of Special
608 Appointment (Eastern Scholar) at Shanghai Institutions of Higher Learning. The authors
609 are grateful to Drs. Hongli Wang and Yaqin Gao for kindly sharing their monoterpene
610 observation data for a sensitivity test.

611

612 *Financial support.* This work was supported by the National Natural Science Foundation
613 of China (Grant # 22022607) and the Science and Technology Commission of Shanghai
614 Municipality (Grant # 19DZ1205004).

615

616 **References:**

617 Alexander, B., Sherwen, T., Holmes, C. D., Fisher, J. A., Chen, Q., Evans, M. J., and Kasibhatla, P.:
618 Global inorganic nitrate production mechanisms: comparison of a global model with nitrate isotope
619 observations, *Atmos. Chem. Phys.*, 20, 3859-3877, doi: 10.5194/acp-20-3859-2020, 2020.

620 Atkinson, R., and Arey, J.: Atmospheric degradation of volatile organic compounds, *Chem. Rev.*, 103,
621 4605-4638, doi, 2003.

622 Bertram, T. H., and Thornton, J. A.: Toward a general parameterization of N₂O₅ reactivity on aqueous
623 particles: the competing effects of particle liquid water, nitrate and chloride, *Atmos. Chem. Phys.*, 9,
624 8351-8363, doi, 2009.

625 Bertram, T. H., Thornton, J. A., Riedel, T. P., Middlebrook, A. M., Bahreini, R., Bates, T. S., Quinn, P.
626 K., and Coffman, D. J.: Direct observations of N₂O₅ reactivity on ambient aerosol particles,
627 *Geophys. Res. Lett.*, 36, doi, 2009.

628 Brown, S. S., and Stutz, J.: Nighttime radical observations and chemistry, *Chem. Soc. Rev.*, 41, 6405-
629 6447, doi, 2012.

630 Calvert, J. G., and Stockwell, W. R.: Acid generation in the troposphere by gas-phase chemistry,
631 *Environ. Sci. Technol.*, 17, 428A-443A, doi, 1983.

- 632 Chan, Y. C., Evans, M. J., He, P., Holmes, C. D., Jaeglé, L., Kasibhatla, P., Liu, X. Y., Sherwen, T.,
633 Thornton, J. A., Wang, X., Xie, Z., Zhai, S., and Alexander, B.: Heterogeneous Nitrate Production
634 Mechanisms in Intense Haze Events in the North China Plain, *J. Geophys. Res.-Atmos.*, 126, doi:
635 10.1029/2021jd034688, 2021.
- 636 Chen, X., Wang, H., Liu, Y., Su, R., Wang, H., Lou, S., and Lu, K.: Spatial characteristics of the
637 nighttime oxidation capacity in the Yangtze River Delta, China, *Atmos. Environ.*, 208, 150-157, doi:
638 10.1016/j.atmosenv.2019.04.012, 2019.
- 639 Chen, X., Wang, H., Lu, K., Li, C., Zhai, T., Tan, Z., Ma, X., Yang, X., Liu, Y., Chen, S., Dong, H., Li,
640 X., Wu, Z., Hu, M., Zeng, L., and Zhang, Y.: Field Determination of Nitrate Formation Pathway in
641 Winter Beijing, *Environ. Sci. Technol.*, 54, 9243-9253, doi: 10.1021/acs.est.0c00972, 2020.
- 642 Ding, A., Fu, C., Yang, X., Sun, J., Zheng, L., Xie, Y., Herrmann, E., Nie, W., Petäjä, T., and Kerminen,
643 V.-M.: Ozone and fine particle in the western Yangtze River Delta: an overview of 1 yr data at the
644 SORPES station, *Atmos. Chem. Phys.*, 13, 5813-5830, doi, 2013.
- 645 Ding, A., Huang, X., Nie, W., Chi, X., Xu, Z., Zheng, L., Xu, Z., Xie, Y., Qi, X., Shen, Y., Sun, P.,
646 Wang, J., Wang, L., Sun, J., Yang, X.-Q., Qin, W., Zhang, X., Cheng, W., Liu, W., Pan, L., and Fu,
647 C.: Significant reduction of PM_{2.5} in eastern China due to regional-scale emission control: evidence
648 from SORPES in 2011–2018, *Atmos. Chem. Phys.*, 19, 11791-11801, doi: 10.5194/acp-19-11791-
649 2019, 2019.
- 650 Duan, J., Huang, R.-J., Li, Y., Chen, Q., Zheng, Y., Chen, Y., Lin, C., Ni, H., Wang, M., Ovadnevaite,
651 J., Ceburnis, D., Chen, C., Worsnop, D. R., Hoffmann, T., O'Dowd, C., and Cao, J.: Summertime and
652 wintertime atmospheric processes of secondary aerosol in Beijing, *Atmos. Chem. Phys.*, 20, 3793-
653 3807, doi: 10.5194/acp-20-3793-2020, 2020.
- 654 Fang, Y., Ye, C., Wang, J., Wu, Y., Hu, M., Lin, W., Xu, F., and Zhu, T.: Relative humidity and O₃
655 concentration as two prerequisites for sulfate formation, *Atmos. Chem. Phys.*, 19, 12295-12307, doi:
656 10.5194/acp-19-12295-2019, 2019.
- 657 Finlayson-Pitts, B. J., Ezell, M. J., and Pitts, J. N.: Formation of chemically active chlorine compounds
658 by reactions of atmospheric NaCl particles with gaseous N₂O₅ and ClONO₂, *Nature*, 337, 241-244,
659 doi: 10.1038/337241a0, 1989.
- 660 Fountoukis, C., and Nenes, A.: ISORROPIA II: a computationally efficient thermodynamic equilibrium
661 model for K⁺-Ca²⁺-Mg²⁺-NH₄⁺-Na⁺-SO₄²⁻-NO₃-Cl⁻-H₂O aerosols, *Atmos. Chem. Phys.*, 7, 4639-
662 4659, doi, 2007.
- 663 Fu, X., Wang, T., Gao, J., Wang, P., Liu, Y., Wang, S., Zhao, B., and Xue, L.: Persistent Heavy Winter
664 Nitrate Pollution Driven by Increased Photochemical Oxidants in Northern China, *Environ. Sci.*
665 *Technol.*, 54, 3881-3889, doi: 10.1021/acs.est.9b07248, 2020.
- 666 Guo, H., Xu, L., Bougiatioti, A., Cerully, K. M., Capps, S. L., Hite Jr, J., Carlton, A., Lee, S.-H.,
667 Bergin, M., and Ng, N.: Fine-particle water and pH in the southeastern United States, *Atmos. Chem.*
668 *Phys.*, 15, 5211-5228, doi, 2015.
- 669 Guo, H., Sullivan, A. P., Campuzano - Jost, P., Schroder, J. C., Lopez - Hilfiker, F. D., Dibb, J. E.,
670 Jimenez, J. L., Thornton, J. A., Brown, S. S., and Nenes, A.: Fine particle pH and the partitioning of
671 nitric acid during winter in the northeastern United States, *J. Geophys. Res.-Atmos.*, 121, 10,355-
672 310,376, doi, 2016.
- 673 Guo, H., Otjes, R., Schlag, P., Kiendler-Scharr, A., Nenes, A., and Weber, R. J.: Effectiveness of
674 ammonia reduction on control of fine particle nitrate, *Atmos. Chem. Phys.*, 18, 12241-12256, doi,
675 2018.
- 676 Han, C., Yang, W., Wu, Q., Yang, H., and Xue, X.: Heterogeneous photochemical conversion of NO₂ to
677 HONO on the humic acid surface under simulated sunlight, *Environ. Sci. Technol.*, 50, 5017-5023,
678 doi, 2016.
- 679 He, P., Xie, Z., Chi, X., Yu, X., Fan, S., Kang, H., Liu, C., and Zhan, H.: Atmospheric Δ¹⁷O(NO₃)
680 reveals nocturnal chemistry dominates nitrate production in Beijing haze, *Atmos. Chem. Phys.*, 18,
681 14465-14476, doi: 10.5194/acp-18-14465-2018, 2018.
- 682 Hennigan, C., Izumi, J., Sullivan, A., Weber, R., and Nenes, A.: A critical evaluation of proxy methods
683 used to estimate the acidity of atmospheric particles, *Atmos. Chem. Phys.*, 15, 2775-2790, doi, 2015.
- 684 Hua, Y., Cheng, Z., Wang, S., Jiang, J., Chen, D., Cai, S., Fu, X., Fu, Q., Chen, C., and Xu, B.:
685 Characteristics and source apportionment of PM_{2.5} during a fall heavy haze episode in the Yangtze
686 River Delta of China, *Atmos. Environ.*, 123, 380-391, doi, 2015.

687 Huang, R.-J., He, Y., Duan, J., Li, Y., Chen, Q., Zheng, Y., Chen, Y., Hu, W., Lin, C., and Ni, H.:
688 Contrasting sources and processes of particulate species in haze days with low and high relative
689 humidity in wintertime Beijing, *Atmos. Chem. Phys.*, 20, 9101-9114, doi, 2020.

690 Huang, R. J., Zhang, Y. L., Bozzetti, C., Ho, K. F., Cao, J. J., Han, Y. M., Daellenbach, K. R., Slowik, J.
691 G., Platt, S. M., Canonaco, F., Zotter, P., Wolf, R., Pieber, S. M., Bruns, E. A., Crippa, M., Ciarelli,
692 G., Piazzalunga, A., Schwikowski, M., Abbaszade, G., Schnelle-Kreis, J., Zimmermann, R., An, Z.
693 S., Szidat, S., Baltensperger, U., El Haddad, I., and Prevot, A. S. H.: High secondary aerosol
694 contribution to particulate pollution during haze events in China, *Nature*, 514, 218-222, doi, 2014.

695 Huang, X., Ding, A., Gao, J., Zheng, B., Zhou, D., Qi, X., Tang, R., Wang, J., Ren, C., and Nie, W.:
696 Enhanced secondary pollution offset reduction of primary emissions during COVID-19 lockdown in
697 China, *Natl. Sci. Rev.*, 8, nwaal37, doi, 2021.

698 Jenkin, M., Young, J., and Rickard, A.: The MCM v3.3.1 degradation scheme for isoprene, *Atmos.*
699 *Chem. Phys.*, 15, 11433-11459, doi, 2015.

700 Kleffmann, J., Becker, K., and Wiesen, P.: Heterogeneous NO₂ conversion processes on acid surfaces:
701 possible atmospheric implications, *Atmos. Environ.*, 32, 2721-2729, doi, 1998.

702 Kong, L., Yang, Y., Zhang, S., Zhao, X., Du, H., Fu, H., Zhang, S., Cheng, T., Yang, X., and Chen, J.:
703 Observations of linear dependence between sulfate and nitrate in atmospheric particles, *J. Geophys.*
704 *Res.-Atmos.*, 119, 341-361, doi, 2014.

705 Kong, L., Feng, M., Liu, Y., Zhang, Y., Zhang, C., Li, C., Qu, Y., An, J., Liu, X., Tan, Q., Cheng, N.,
706 Deng, Y., Zhai, R., and Wang, Z.: Elucidating the pollution characteristics of nitrate, sulfate and
707 ammonium in PM_{2.5} in Chengdu, southwest China, based on 3-year measurements, *Atmos. Chem.*
708 *Phys.*, 20, 11181-11199, doi: 10.5194/acp-20-11181-2020, 2020.

709 Kurtenbach, R., Becker, K., Gomes, J., Kleffmann, J., Lörzer, J., Spittler, M., Wiesen, P., Ackermann,
710 R., Geyer, A., and Platt, U.: Investigations of emissions and heterogeneous formation of HONO in a
711 road traffic tunnel, *Atmos. Environ.*, 35, 3385-3394, doi, 2001.

712 Le, T., Wang, Y., Liu, L., Yang, J., Yung, Y. L., Li, G., and Seinfeld, J. H.: Unexpected air pollution
713 with marked emission reductions during the COVID-19 outbreak in China, *Science*, 369, 702-706,
714 doi, 2020.

715 Lee, Y., and Schwartz, S. E.: Kinetics of oxidation of aqueous sulfur (IV) by nitrogen dioxide,
716 Precipitation Scavenging, Dry Deposition and Resuspension, 1, 453-470, doi, 1983.

717 Lelieveld, J., Evans, J. S., Fnais, M., Giannadaki, D., and Pozzer, A.: The contribution of outdoor air
718 pollution sources to premature mortality on a global scale, *Nature*, 525, 367-+, doi, 2015.

719 Li, H., Zhang, Q., Zheng, B., Chen, C., Wu, N., Guo, H., Zhang, Y., Zheng, Y., Li, X., and He, K.:
720 Nitrate-driven urban haze pollution during summertime over the North China Plain, *Atmos. Chem.*
721 *Phys.*, 18, 5293-5306, doi: 10.5194/acp-18-5293-2018, 2018.

722 Li, H., Cheng, J., Zhang, Q., Zheng, B., Zhang, Y., Zheng, G., and He, K.: Rapid transition in winter
723 aerosol composition in Beijing from 2014 to 2017: response to clean air actions, *Atmos. Chem.*
724 *Phys.*, 19, 11485-11499, doi, 2019a.

725 Li, K., Jacob, D. J., Liao, H., Zhu, J., Shah, V., Shen, L., Bates, K. H., Zhang, Q., and Zhai, S.: A two-
726 pollutant strategy for improving ozone and particulate air quality in China, *Nat. Geosci.*, 12, 906-
727 910, doi, 2019b.

728 Li, M., Wang, T., Xie, M., Li, S., Zhuang, B., Huang, X., Chen, P., Zhao, M., and Liu, J.: Formation
729 and evolution mechanisms for two extreme haze episodes in the Yangtze River Delta region of China
730 during winter 2016, *J. Geophys. Res.-Atmos.*, 124, 3607-3623, doi, 2019c.

731 Lin, Y.-C., Zhang, Y.-L., Fan, M.-Y., and Bao, M.: Heterogeneous formation of particulate nitrate under
732 ammonium-rich regimes during the high-PM_{2.5} events in Nanjing, China, *Atmos. Chem. Phys.*, 20,
733 3999-4011, doi: 10.5194/acp-20-3999-2020, 2020.

734 Liu, L., Zhang, J., Du, R., Teng, X., Hu, R., Yuan, Q., Tang, S., Ren, C., Huang, X., and Xu, L.:
735 Chemistry of atmospheric fine particles during the COVID-19 pandemic in a megacity of Eastern
736 China, *Geophys. Res. Lett.*, 48, 2020GL091611, doi, 2021.

737 Liu, P., Ye, C., Xue, C., Zhang, C., Mu, Y., and Sun, X.: Formation mechanisms of atmospheric nitrate
738 and sulfate during the winter haze pollution periods in Beijing: gas-phase, heterogeneous and
739 aqueous-phase chemistry, *Atmos. Chem. Phys.*, 20, 4153-4165, doi: 10.5194/acp-20-4153-2020,
740 2020a.

741 Liu, Y., Lu, K., Ma, Y., Yang, X., Zhang, W., Wu, Y., Peng, J., Shuai, S., Hu, M., and Zhang, Y.: Direct

742 emission of nitrous acid (HONO) from gasoline cars in China determined by vehicle chassis
743 dynamometer experiments, *Atmos. Environ.*, 169, 89-96, doi, 2017.

744 Liu, Y., Lu, K., Li, X., Dong, H., Tan, Z., Wang, H., Zou, Q., Wu, Y., Zeng, L., Hu, M., Min, K. E.,
745 Kecorius, S., Wiedensohler, A., and Zhang, Y.: A Comprehensive Model Test of the HONO Sources
746 Constrained to Field Measurements at Rural North China Plain, *Environ. Sci. Technol.*, 53, 3517-
747 3525, doi: 10.1021/acs.est.8b06367, 2019.

748 Liu, Y., and Wang, T.: Worsening urban ozone pollution in China from 2013 to 2017–Part 1: The
749 complex and varying roles of meteorology, *Atmos. Chem. Phys.*, 20, 6305-6321, doi, 2020.

750 Liu, Y. C., Zhang, Y. S., Lian, C. F., Yan, C., Feng, Z. M., Zheng, F. X., Fan, X. L., Chen, Y., Wang, W.
751 G., Chu, B. W., Wang, Y. H., Cai, J., Du, W., Daellenbach, K. R., Kangasluoma, J., Bianchi, F.,
752 Kujansuu, J., Petaja, T., Wang, X. F., Hu, B., Wang, Y. S., Ge, M. F., He, H., and Kulmala, M.: The
753 promotion effect of nitrous acid on aerosol formation in wintertime in Beijing: the possible
754 contribution of traffic-related emissions, *Atmos. Chem. Phys.*, 20, 13023-13040, doi: 10.5194/acp-
755 20-13023-2020, 2020b.

756 Lu, K. D., Fuchs, H., Hofzumahaus, A., Tan, Z. F., Wang, H. C., Zhang, L., Schmitt, S. H., Rohrer, F.,
757 Bohn, B., Broch, S., Dong, H. B., Gkatzelis, G. I., Hohaus, T., Holland, F., Li, X., Liu, Y., Liu, Y. H.,
758 Ma, X. F., Novelli, A., Schlag, P., Shao, M., Wu, Y. S., Wu, Z. J., Zeng, L. M., Hu, M., Kiendler-
759 Schar, A., Wahner, A., and Zhang, Y. H.: Fast Photochemistry in Wintertime Haze: Consequences
760 for Pollution Mitigation Strategies, *Environ. Sci. Technol.*, 53, 10676-10684, doi:
761 10.1021/acs.est.9b02422, 2019.

762 Lu, X., Hong, J., Zhang, L., Cooper, O. R., Schultz, M. G., Xu, X., Wang, T., Gao, M., Zhao, Y., and
763 Zhang, Y.: Severe surface ozone pollution in China: a global perspective, *Environ. Sci. Technol.*
764 *Letts.*, 5, 487-494, doi, 2018.

765 McDuffie, E. E., Womack, C. C., Fibiger, D. L., Dube, W. P., Franchin, A., Middlebrook, A. M.,
766 Goldberger, L., Lee, B., Thornton, J. A., Moravek, A., Murphy, J. G., Baasandorj, M., and Brown, S.
767 S.: On the contribution of nocturnal heterogeneous reactive nitrogen chemistry to particulate matter
768 formation during wintertime pollution events in Northern Utah, *Atmos. Chem. Phys.*, 19, 9287-9308,
769 doi: 10.5194/acp-19-9287-2019, 2019.

770 Mozurkewich, M., and Calvert, J. G.: Reaction probability of N₂O₅ on aqueous aerosols, *J. Geophys.*
771 *Res.-Atmos.*, 93, 15889-15896, doi, 1988.

772 Peng, J. F., Hu, M., Shang, D. J., Wu, Z. J., Du, Z. F., Tan, T. Y., Wang, Y. N., Zhang, F., and Zhang, R.
773 Y.: Explosive Secondary Aerosol Formation during Severe Haze in the North China Plain, *Environ.*
774 *Sci. Technol.*, 55, 2189-2207, doi: 10.1021/acs.est.0c07204, 2021.

775 Romer, P. S., Wooldridge, P. J., Crouse, J. D., Kim, M. J., Wennberg, P. O., Dibb, J. E., Scheuer, E.,
776 Blake, D. R., Meinardi, S., and Brosius, A. L.: Constraints on Aerosol Nitrate Photolysis as a
777 Potential Source of HONO and NO_x, *Environ. Sci. Technol.*, 52, 13738-13746, doi, 2018.

778 Schweitzer, F., Mirabel, P., and George, C.: Multiphase chemistry of N₂O₅, ClNO₂, and BrNO₂, *J. Phys.*
779 *Chem. A*, 102, 3942-3952, doi: DOI 10.1021/jp980748s, 1998.

780 Shao, P. Y., Tian, H. Z., Sun, Y. J., Liu, H. J., Wu, B. B., Liu, S. H., Liu, X. Y., Wu, Y. M., Liang, W. Z.,
781 Wang, Y., Gao, J. J., Xue, Y. F., Bai, X. X., Liu, W., Lin, S. M., and Hu, G. Z.: Characterizing
782 remarkable changes of severe haze events and chemical compositions in multi-size airborne particles
783 (PM₁, PM_{2.5} and PM₁₀) from January 2013 to 2016-2017 winter in Beijing, China, *Atmos. Environ.*,
784 189, 133-144, doi: 10.1016/j.atmosenv.2018.06.038, 2018.

785 Shen, J., Zhao, Q., Cheng, Z., Wang, P., Ying, Q., Liu, J., Duan, Y., and Fu, Q.: Insights into source
786 origins and formation mechanisms of nitrate during winter haze episodes in the Yangtze River Delta,
787 *Sci. Total. Environ.*, 741, 140187, doi: 10.1016/j.scitotenv.2020.140187, 2020.

788 Slater, E. J., Whalley, L. K., Woodward-Massey, R., Ye, C., Lee, J. D., Squires, F., Hopkins, J. R.,
789 Dunmore, R. E., Shaw, M., and Hamilton, J. F.: Elevated levels of OH observed in haze events
790 during wintertime in central Beijing, *Atmos. Chem. Phys.*, 20, 14847-14871, doi, 2020.

791 Su, X., Tie, X., Li, G., Cao, J., Huang, R., Feng, T., Long, X., and Xu, R.: Effect of hydrolysis of N₂O₅
792 on nitrate and ammonium formation in Beijing China: WRF-Chem model simulation, *Sci. Total.*
793 *Environ.*, 579, 221-229, doi, 2017.

794 Sun, P., Nie, W., Chi, X., Xie, Y., Huang, X., Xu, Z., Qi, X., Xu, Z., Wang, L., Wang, T., Zhang, Q., and
795 Ding, A.: Two years of online measurement of fine particulate nitrate in the western Yangtze River
796 Delta: influences of thermodynamics and N₂O₅ hydrolysis, *Atmos. Chem. Phys.*, 18, 17177-17190,
797 doi: 10.5194/acp-18-17177-2018, 2018.

798 Tan, Z., Fuchs, H., Lu, K., Hofzumahaus, A., Bohn, B., Broch, S., Dong, H., Gomm, S., Häseler, R.,
799 and He, L.: Radical chemistry at a rural site (Wangdu) in the North China Plain: observation and
800 model calculations of OH, HO₂ and RO₂ radicals, *Atmos. Chem. Phys.*, 17, 663-690, doi, 2017.

801 Tao, J., Zhang, L. M., Cao, J. J., and Zhang, R. J.: A review of current knowledge concerning PM_{2.5}
802 chemical composition, aerosol optical properties and their relationships across China, *Atmos. Chem.*
803 *Phys.*, 17, 9485-9518, doi: 10.5194/acp-17-9485-2017, 2017.

804 Tao, Y., Ye, X., Ma, Z., Xie, Y., Wang, R., Chen, J., Yang, X., and Jiang, S.: Insights into different
805 nitrate formation mechanisms from seasonal variations of secondary inorganic aerosols in Shanghai,
806 *Atmos. Environ.*, 145, 1-9, doi: 10.1016/j.atmosenv.2016.09.012, 2016.

807 Thornton, J. A., and Abbatt, J. P. D.: N₂O₅ reaction on submicron sea salt aerosol: Kinetics, products,
808 and the effect of surface active organics, *J. Phys. Chem. A*, 109, 10004-10012, doi:
809 10.1021/jp054183t, 2005.

810 Tian, J., Wang, Q., Zhang, Y., Yan, M., Liu, H., Zhang, N., Ran, W., and Cao, J.: Impacts of primary
811 emissions and secondary aerosol formation on air pollution in an urban area of China during the
812 COVID-19 lockdown, *Environ. Int.*, 150, 106426, doi, 2021.

813 Trinh, H. T., Imanishi, K., Morikawa, T., Hagino, H., and Takenaka, N.: Gaseous nitrous acid (HONO)
814 and nitrogen oxides (NO_x) emission from gasoline and diesel vehicles under real-world driving test
815 cycles, *J. Air. Waste. Manage.*, 67, 412-420, doi, 2017.

816 von Schneidmesser, E., Monks, P. S., Allan, J. D., Bruhwiler, L., Forster, P., Fowler, D., Lauer, A.,
817 Morgan, W. T., Paasonen, P., Righi, M., Sindelarova, K., and Sutton, M. A.: Chemistry and the
818 Linkages between Air Quality and Climate Change, *Chem. Rev.*, 115, 3856-3897, doi:
819 10.1021/acs.chemrev.5b00089, 2015.

820 Wagner, N., Riedel, T., Young, C., Bahreini, R., Brock, C., Dubé, W., Kim, S., Middlebrook, A.,
821 Öztürk, F., and Roberts, J.: N₂O₅ uptake coefficients and nocturnal NO₂ removal rates determined
822 from ambient wintertime measurements, *J. Geophys. Res.-Atmos.*, 118, 9331-9350, doi, 2013.

823 Wang, H., Lu, K., Chen, X., Zhu, Q., Chen, Q., Guo, S., Jiang, M., Li, X., Shang, D., Tan, Z., Wu, Y.,
824 Wu, Z., Zou, Q., Zheng, Y., Zeng, L., Zhu, T., Hu, M., and Zhang, Y.: High N₂O₅ Concentrations
825 Observed in Urban Beijing: Implications of a Large Nitrate Formation Pathway, *Environ. Sci.*
826 *Technol. Lett.*, 4, 416-420, doi: 10.1021/acs.estlett.7b00341, 2017.

827 Wang, J., Li, J., Ye, J., Zhao, J., Wu, Y., Hu, J., Liu, D., Nie, D., Shen, F., Huang, X., Huang, D. D., Ji,
828 D., Sun, X., Xu, W., Guo, J., Song, S., Qin, Y., Liu, P., Turner, J. R., Lee, H. C., Hwang, S., Liao, H.,
829 Martin, S. T., Zhang, Q., Chen, M., Sun, Y., Ge, X., and Jacob, D. J.: Fast sulfate formation from
830 oxidation of SO₂ by NO₂ and HONO observed in Beijing haze, *Nat. Commun.*, 11, 2844, doi:
831 10.1038/s41467-020-16683-x, 2020a.

832 Wang, W., Yu, J., Cui, Y., He, J., Xue, P., Cao, W., Ying, H., Gao, W., Yan, Y., Hu, B., Xin, J., Wang, L.,
833 Liu, Z., Sun, Y., Ji, D., and Wang, Y.: Characteristics of fine particulate matter and its sources in an
834 industrialized coastal city, Ningbo, Yangtze River Delta, China, *Atmos. Res.*, 203, 105-117, doi:
835 10.1016/j.atmosres.2017.11.033, 2018.

836 Wang, Y., Zhang, R., and Saravanan, R.: Asian pollution climatically modulates mid-latitude cyclones
837 following hierarchical modelling and observational analysis, *Nat. Commun.*, 5, 1-7, doi, 2014.

838 Wang, Y., Chen, Y., Wu, Z., Shang, D., Bian, Y., Du, Z., Schmitt, S. H., Su, R., Gkatzelis, G. I., Schlag,
839 P., Hohaus, T., Voliotis, A., Lu, K., Zeng, L., Zhao, C., Alfarra, M. R., McFiggans, G., Wiedensohler,
840 A., Kiendler-Scharr, A., Zhang, Y., and Hu, M.: Mutual promotion between aerosol particle liquid
841 water and particulate nitrate enhancement leads to severe nitrate-dominated particulate matter
842 pollution and low visibility, *Atmos. Chem. Phys.*, 20, 2161-2175, doi: 10.5194/acp-20-2161-2020,
843 2020b.

844 Wayne, R. P., Barnes, I., Biggs, P., Burrows, J., Canosa-Mas, C., Hjorth, J., Le Bras, G., Moortgat, G.,
845 Perner, D., and Poulet, G.: The nitrate radical: Physics, chemistry, and the atmosphere, *Atmos.*
846 *Environ.. Part A. General Topics*, 25, 1-203, doi, 1991.

847 Wen, L., Chen, J., Yang, L., Wang, X., Xu, C., Sui, X., Yao, L., Zhu, Y., Zhang, J., and Zhu, T.:
848 Enhanced formation of fine particulate nitrate at a rural site on the North China Plain in summer:
849 The important roles of ammonia and ozone, *Atmos. Environ.*, 101, 294-302, doi, 2015.

850 Wen, L., Xue, L., Wang, X., Xu, C., Chen, T., Yang, L., Wang, T., Zhang, Q., and Wang, W.:
851 Summertime fine particulate nitrate pollution in the North China Plain: increasing trends, formation
852 mechanisms and implications for control policy, *Atmos. Chem. Phys.*, 18, 11261-11275, doi:
853 10.5194/acp-18-11261-2018, 2018.

854 Wolfe, G. M., Marvin, M. R., Roberts, S. J., Travis, K. R., and Liao, J.: The framework for 0-D
855 atmospheric modeling (FOAM) v3.1, *Geosci. Model. Dev.*, 9, 3309-3319, doi, 2016.

856 Wong, K., Oh, H.-J., Lefer, B., Rappenglück, B., and Stutz, J.: Vertical profiles of nitrous acid in the
857 nocturnal urban atmosphere of Houston, TX, *Atmos. Chem. Phys.*, 11, 3595-3609, doi, 2011.

858 Wong, K., Tsai, C., Lefer, B., Grossberg, N., and Stutz, J.: Modeling of daytime HONO vertical
859 gradients during SHARP 2009, *Atmos. Chem. Phys.*, 13, 3587-3601, doi, 2013.

860 Xie, Y., Ding, A., Nie, W., Mao, H., Qi, X., Huang, X., Xu, Z., Kerminen, V. M., Petäjä, T., and Chi, X.:
861 Enhanced sulfate formation by nitrogen dioxide: Implications from in situ observations at the
862 SORPES station, *J. Geophys. Res.-Atmos.*, 120, 12679-12694, doi, 2015.

863 Xie, Y., Wang, G., Wang, X., Chen, J., Chen, Y., Tang, G., Wang, L., Ge, S., Xue, G., Wang, Y., and
864 Gao, J.: Nitrate-dominated PM_{2.5} and elevation of particle pH observed in urban Beijing during the
865 winter of 2017, *Atmos. Chem. Phys.*, 20, 5019-5033, doi: 10.5194/acp-20-5019-2020, 2020.

866 Xu, Q., Wang, S., Jiang, J., Bhattarai, N., Li, X., Chang, X., Qiu, X., Zheng, M., Hua, Y., and Hao, J.:
867 Nitrate dominates the chemical composition of PM_{2.5} during haze event in Beijing, China, *Sci. Total.
868 Environ.*, 689, 1293-1303, doi, 2019.

869 Xue, C., Zhang, C., Ye, C., Liu, P., Catoire, V., Krysztofiak, G., Chen, H., Ren, Y., Zhao, X., Wang, J.,
870 Zhang, F., Zhang, C., Zhang, J., An, J., Wang, T., Chen, J., Kleffmann, J., Mellouki, A., and Mu, Y.:
871 HONO Budget and Its Role in Nitrate Formation in the Rural North China Plain, *Environ. Sci.
872 Technol.*, 54, 11048-11057, doi: 10.1021/acs.est.0c01832, 2020.

873 Yang, G., Liu, Y., and Li, X.: Spatiotemporal distribution of ground-level ozone in China at a city level,
874 *Sci. Rep.*, 10, 1-12, doi, 2020.

875 Ye, C., Zhou, X., Pu, D., Stutz, J., Festa, J., Spolaor, M., Tsai, C., Cantrell, C., Mauldin, R. L., and
876 Campos, T.: Rapid cycling of reactive nitrogen in the marine boundary layer, *Nature*, 532, 489-491,
877 doi, 2016.

878 Ye, S., Ma, T., Duan, F., Li, H., He, K., Xia, J., Yang, S., Zhu, L., Ma, Y., and Huang, T.: Characteristics
879 and formation mechanisms of winter haze in Changzhou, a highly polluted industrial city in the
880 Yangtze River Delta, China, *Environ. Pollut.*, 253, 377-383, doi, 2019.

881 Ye, Z., Liu, J., Gu, A., Feng, F., Liu, Y., Bi, C., Xu, J., Li, L., Chen, H., Chen, Y., Dai, L., Zhou, Q., and
882 Ge, X.: Chemical characterization of fine particulate matter in Changzhou, China, and source
883 apportionment with offline aerosol mass spectrometry, *Atmos. Chem. Phys.*, 17, 2573-2592, doi:
884 10.5194/acp-17-2573-2017, 2017.

885 Yu, C., Wang, Z., Xia, M., Fu, X., Wang, W., Tham, Y. J., Chen, T., Zheng, P., Li, H., Shan, Y., Wang,
886 X., Xue, L., Zhou, Y., Yue, D., Ou, Y., Gao, J., Lu, K., Brown, S. S., Zhang, Y., and Wang, T.:
887 Heterogeneous N₂O₅ reactions on atmospheric aerosols at four Chinese sites: improving model
888 representation of uptake parameters, *Atmos. Chem. Phys.*, 20, 4367-4378, doi: 10.5194/acp-20-
889 4367-2020, 2020a.

890 Yu, Y., Xu, H., Jiang, Y., Chen, F., and Liu, D.: A modeling study of PM_{2.5} transboundary transport
891 during a winter severe haze episode in southern Yangtze River Delta, China, *Atmos. Res.*, 248,
892 105159, doi, 2020b.

893 Yun, H., Wang, W., Wang, T., Xia, M., Yu, C., Wang, Z., Poon, S. C., Yue, D., and Zhou, Y.: Nitrate
894 formation from heterogeneous uptake of dinitrogen pentoxide during a severe winter haze in
895 southern China, *Atmos. Chem. Phys.*, 18, 17515-17527, doi, 2018.

896 Zare, A., Romer, P. S., Nguyen, T., Keutsch, F. N., Skog, K., and Cohen, R. C.: A comprehensive
897 organic nitrate chemistry: insights into the lifetime of atmospheric organic nitrates, *Atmos. Chem.
898 Phys.*, 18, 15419-15436, doi: 10.5194/acp-18-15419-2018, 2018.

899 Zhai, S., Jacob, D. J., Wang, X., Liu, Z., Wen, T., Shah, V., Li, K., Moch, J. M., Bates, K. H., Song, S.,
900 Shen, L., Zhang, Y., Luo, G., Yu, F., Sun, Y., Wang, L., Qi, M., Tao, J., Gui, K., Xu, H., Zhang, Q.,
901 Zhao, T., Wang, Y., Lee, H. C., Choi, H., and Liao, H.: Control of particulate nitrate air pollution in
902 China, *Nat. Geosci.*, 14, 389-395, doi: 10.1038/s41561-021-00726-z, 2021.

903 Zhang, Q., Zheng, Y. X., Tong, D., Shao, M., Wang, S. X., Zhang, Y. H., Xu, X. D., Wang, J. N., He,
904 H., Liu, W. Q., Ding, Y. H., Lei, Y., Li, J. H., Wang, Z. F., Zhang, X. Y., Wang, Y. S., Cheng, J., Liu,
905 Y., Shi, Q. R., Yan, L., Geng, G. N., Hong, C. P., Li, M., Liu, F., Zheng, B., Cao, J. J., Ding, A. J.,
906 Gao, J., Fu, Q. Y., Huo, J. T., Liu, B. X., Liu, Z. R., Yang, F. M., He, K. B., and Hao, J. M.: Drivers
907 of improved PM_{2.5} air quality in China from 2013 to 2017, *Proc. Natl. Acad. Sci. U.S.A.*, 116,
908 24463-24469, doi: 10.1073/pnas.1907956116, 2019.

909 Zhang, T., Shen, Z., Su, H., Liu, S., Zhou, J., Zhao, Z., Wang, Q., Prévôt, A., and Cao, J.: Effects of

910 Aerosol Water Content on the formation of secondary inorganic aerosol during a Winter Heavy PM_{2.5}
911 Pollution Episode in Xi'an, China, *Atmos. Environ.*, 252, 118304, doi, 2021.

912 Zhang, Y.-L., and Cao, F.: Fine particulate matter (PM_{2.5}) in China at a city level, *Sci. Rep.*, 5, 1-12,
913 doi, 2015.

914 Zhao, P., Dong, F., He, D., Zhao, X., Zhang, X., Zhang, W., Yao, Q., and Liu, H.: Characteristics of
915 concentrations and chemical compositions for PM_{2.5} in the region of Beijing, Tianjin, and Hebei,
916 China, *Atmos. Chem. Phys.*, 13, 4631-4644, doi, 2013.

917 Zhao, Q., Huo, J., Yang, X., Fu, Q., Duan, Y., Liu, Y., Lin, Y., and Zhang, Q.: Chemical characterization
918 and source identification of submicron aerosols from a year-long real-time observation at a rural site
919 of Shanghai using an Aerosol Chemical Speciation Monitor, *Atmos. Res.*, 246, doi:
920 10.1016/j.atmosres.2020.105154, 2020a.

921 Zhao, Y. B., Zhang, K., Xu, X. T., Shen, H. Z., Zhu, X., Zhang, Y. X., Hu, Y. T., and Shen, G. F.:
922 Substantial Changes in Nitrogen Dioxide and Ozone after Excluding Meteorological Impacts during
923 the COVID-19 Outbreak in Mainland China, *Environ. Sci. Technol. Lett.*, 7, 402-408, doi, 2020b.

924 Zheng, B., Tong, D., Li, M., Liu, F., Hong, C. P., Geng, G. N., Li, H. Y., Li, X., Peng, L. Q., Qi, J., Yan,
925 L., Zhang, Y. X., Zhao, H. Y., Zheng, Y. X., He, K. B., and Zhang, Q.: Trends in China's
926 anthropogenic emissions since 2010 as the consequence of clean air actions, *Atmos. Chem. Phys.*,
927 18, 14095-14111, doi: 10.5194/acp-18-14095-2018, 2018.

928 Zheng, H., Kong, S., Chen, N., Yan, Y., Liu, D., Zhu, B., Xu, K., Cao, W., Ding, Q., Lan, B., Zhang, Z.,
929 Zheng, M., Fan, Z., Cheng, Y., Zheng, S., Yao, L., Bai, Y., Zhao, T., and Qi, S.: Significant changes
930 in the chemical compositions and sources of PM_{2.5} in Wuhan since the city lockdown as COVID-19,
931 *Sci. Total. Environ.*, 739, 140000, doi: 10.1016/j.scitotenv.2020.140000, 2020.

932 Zhong, H., Huang, R.-J., Chang, Y., Duan, J., Lin, C., and Chen, Y.: Enhanced formation of secondary
933 organic aerosol from photochemical oxidation during the COVID-19 lockdown in a background site
934 in Northwest China, *Sci. Total. Environ.*, 778, 144947, doi, 2021.

935

936

937 Table 1 Parameterization of the formation and removal pathways of HONO added to the model.

Mechanism	Parametrization	Max	Min	Ref
$\text{NO}_2 + \text{aerosol} \rightarrow 0.5\text{HONO} + 0.5\text{HNO}_3$	$\gamma\text{NO}_2 = 2 \times 10^{-6}$	1×10^{-5}	4×10^{-7}	a-d
$\text{NO}_2 + \text{ground} \rightarrow \text{HONO}$	$\gamma\text{NO}_2 = 2 \times 10^{-6}$	1×10^{-5}	4×10^{-7}	a-d
$\text{NO}_2 + \text{aerosol} + \text{hv} \rightarrow \text{HONO}$	$\gamma\text{NO}_2 = 2 \times 10^{-5} \times j\text{NO}_2 / j\text{NO}_2\text{noon}^*$	1×10^{-4}	4×10^{-6}	b, e-g
$\text{NO}_2 + \text{ground} + \text{hv} \rightarrow \text{HONO}$	$\gamma\text{NO}_2 = 2 \times 10^{-5} \times j\text{NO}_2 / j\text{NO}_2\text{noon}^*$	1×10^{-4}	4×10^{-6}	b, e-g
$\text{pNO}_3 + \text{hv} \rightarrow \text{HONO}$	$j\text{NO}_3 = j\text{HNO}_3 \times 30$	100	1	h, i
Vehicular emission	$\text{HONO}/\text{NO}_x = 0.8\%$	0.18%	1.6%	j-l
$\text{NO}_2 + \text{SO}_2 + \text{aerosol} \rightarrow \text{HONO} + \text{SO}_4^{2-}$	$k_{aq} = 1.4 \times 10^5 \text{ M}^{-1} \text{ s}^{-1}$ (pH < 5); $2 \times 10^6 \text{ M}^{-1} \text{ s}^{-1}$ (pH > 6)			m, n
HONO deposition	$k_{dep} = \exp^{(23920/T-91.5)}/\text{PBL}$			a

938 *The value of $j\text{NO}_2\text{noon}$ used in the model was 0.005 s^{-1} ; References: ^aXue et al. (2020); ^bLiu et al.
 939 (2019); ^cWong et al. (2011); ^dKleffmann et al. (1998); ^eWong et al. (2013); ^fZare et al. (2018); ^gHan
 940 et al. (2016); ^hRomer et al. (2018); ⁱYe et al. (2016); ^jKurtenbach et al. (2001); ^kLiu et al. (2017),
 941 ^lTrinh et al. (2017); ^mLee and Schwartz (1983); ⁿWang et al. (2020a).

942

943

944

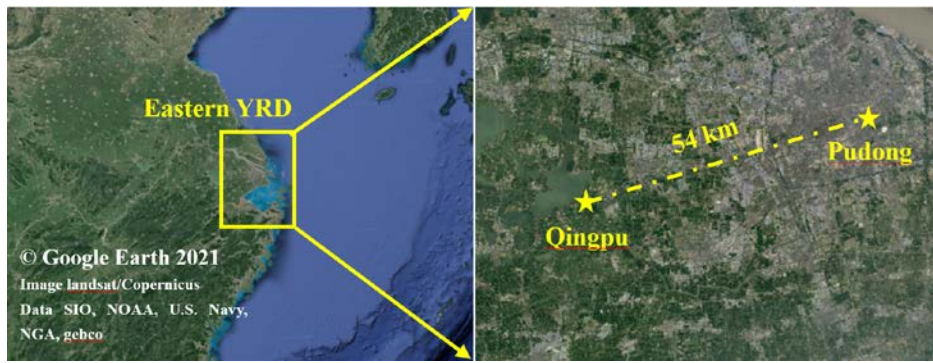
945 Table 2 Concentrations (average \pm standard deviation) of $\text{PM}_{2.5}$, particulate nitrate, NO_x , and O_3 , as
 946 well as temperature and RH at Qingpu and Pudong sites in the winter of 2018 and 2019.

	Sites			
	Qingpu-2018	Pudong-2018	Qingpu-2019	Pudong-2019
$\text{PM}_{2.5}$ ($\mu\text{g m}^{-3}$)	50.0 ± 34.8	40.9 ± 32.5	58.6 ± 37.2	49.5 ± 35.3
NO_3^- ($\mu\text{g m}^{-3}$)	14.9 ± 12.8	11.9 ± 12.2	17.0 ± 14.8	13.2 ± 12.0
NO_x (ppb)	29.6 ± 31.1	27.5 ± 24.4	35.1 ± 33.1	26.9 ± 21.3
O_3 (ppb)	19.1 ± 12.7	18.8 ± 10.4	21.7 ± 14.3	22.3 ± 12.0
Temperature ($^\circ\text{C}$)	6.6 ± 4.4	7.3 ± 4.2	7.5 ± 4.2	8.2 ± 3.8
RH (%)	80 ± 17	78 ± 18	80 ± 17	79 ± 20

947

948

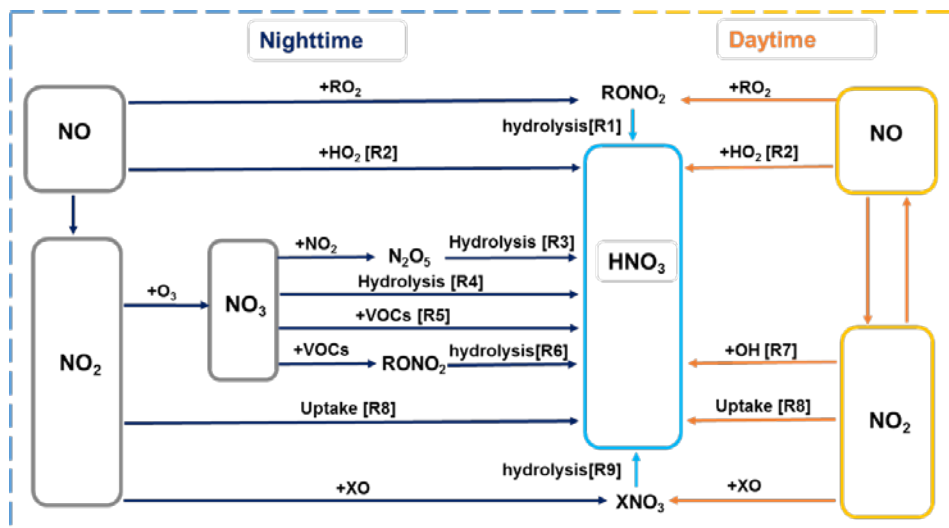
949



950

951 Figure 1 Map of the eastern YRD region and the two observation sites, i.e., Qingpu (suburban and
952 regional) and Pudong (urban).

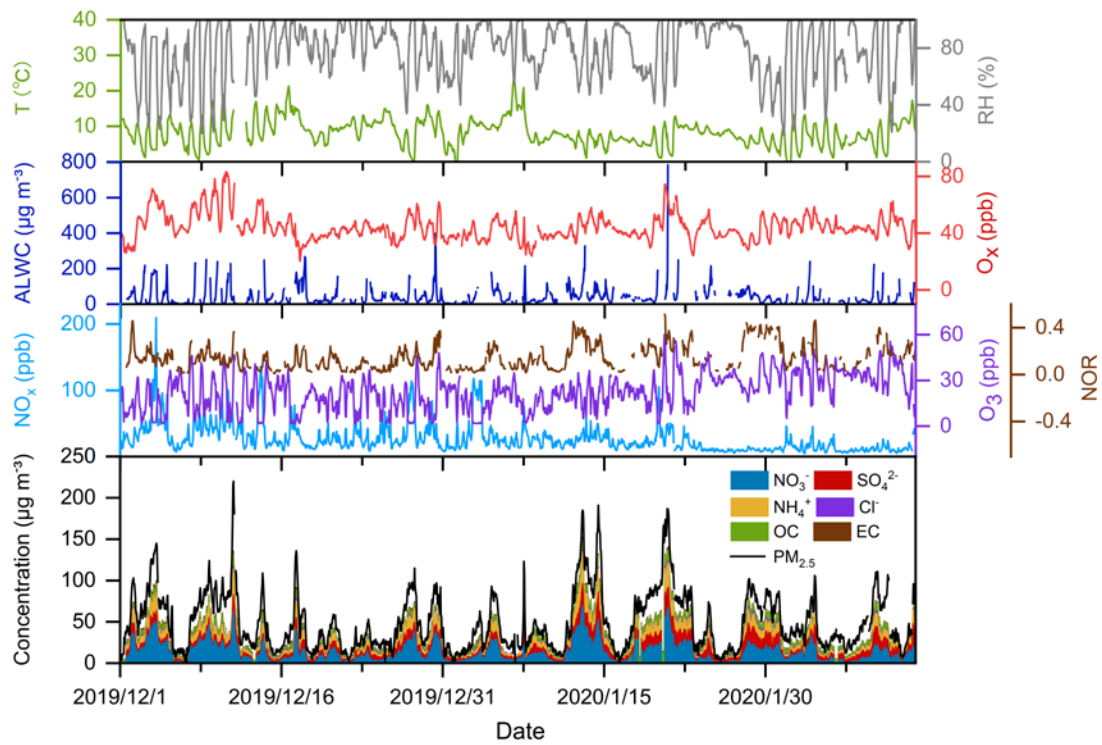
953



954

955 Figure 2 Simplified HNO₃ formation mechanisms in the troposphere. X represents Cl, Br, and I.

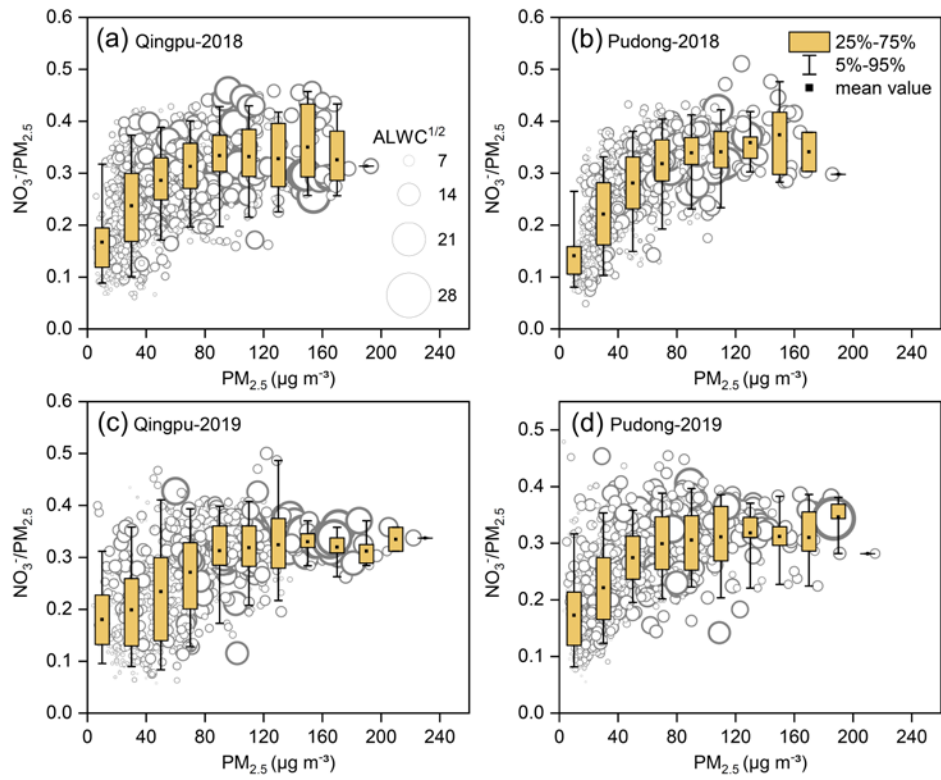
956



957

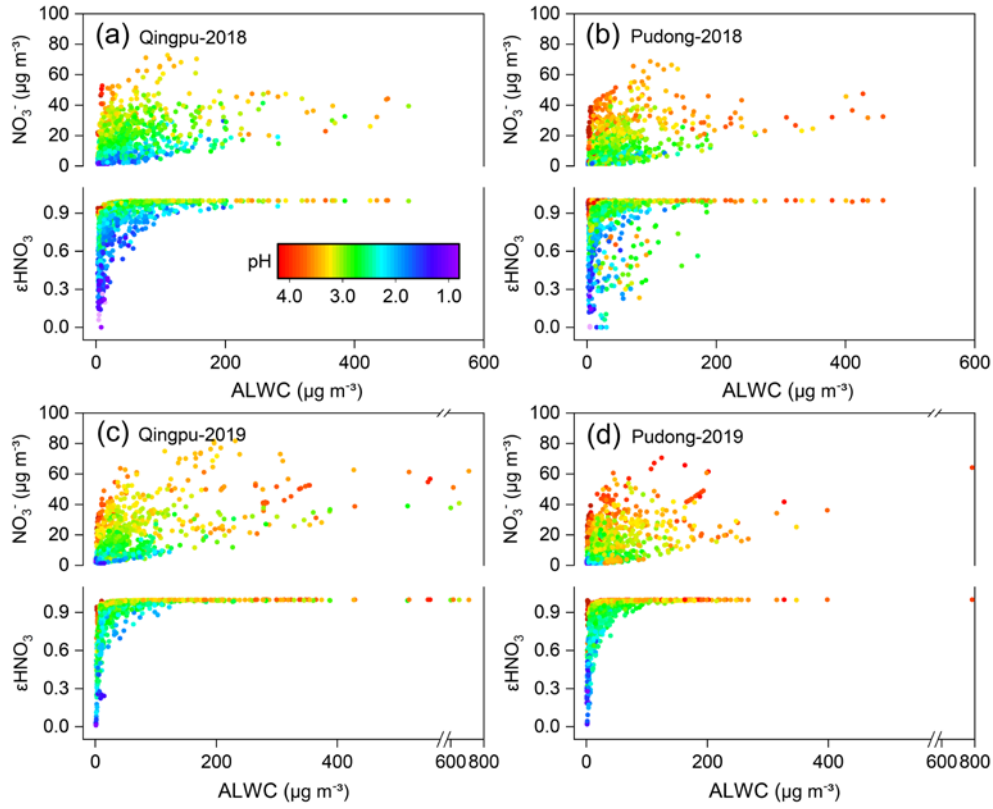
958 Figure 3 Time series of temperature, relative humidity (RH), aerosol liquid water content (ALWC),
 959 NO_x , O_3 , O_x , nitrogen oxidation ratio (NOR), as well as $\text{PM}_{2.5}$ and major particulate compositions
 960 at the Pudong site in the winter of 2019.

961



962
 963
 964
 965
 966

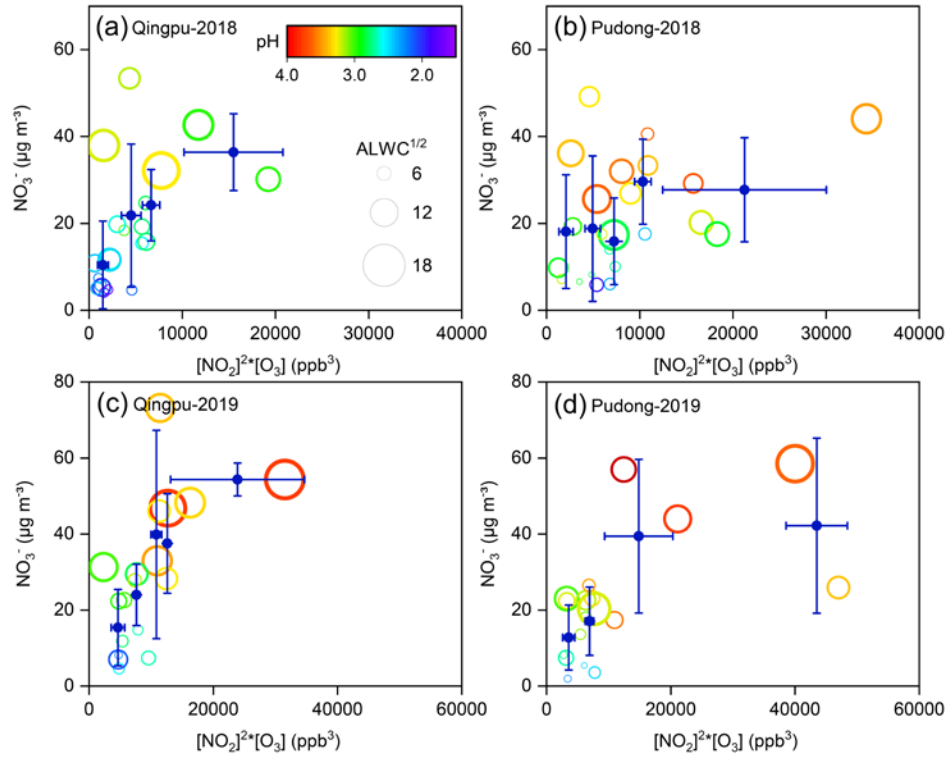
Figure 4 Mass ratio of nitrate to PM_{2.5} as a function of PM_{2.5} concentration at (a, c) Qingpu and (b, d) Pudong sites in the winter of 2018 and 2019. The circles represent the measured ratio of $\text{NO}_3^-/\text{PM}_{2.5}$, and their area is linearly scaled with square root of ALWC.



967

968 Figure 5 Particulate nitrate concentration and its fraction to total nitrate (ϵHNO_3) as a function of
 969 ALWC and aerosol pH at (a, c) Qingpu and (b, d) Pudong sites in the winter of 2018 and 2019. The
 970 circles are colored according to aerosol pH.

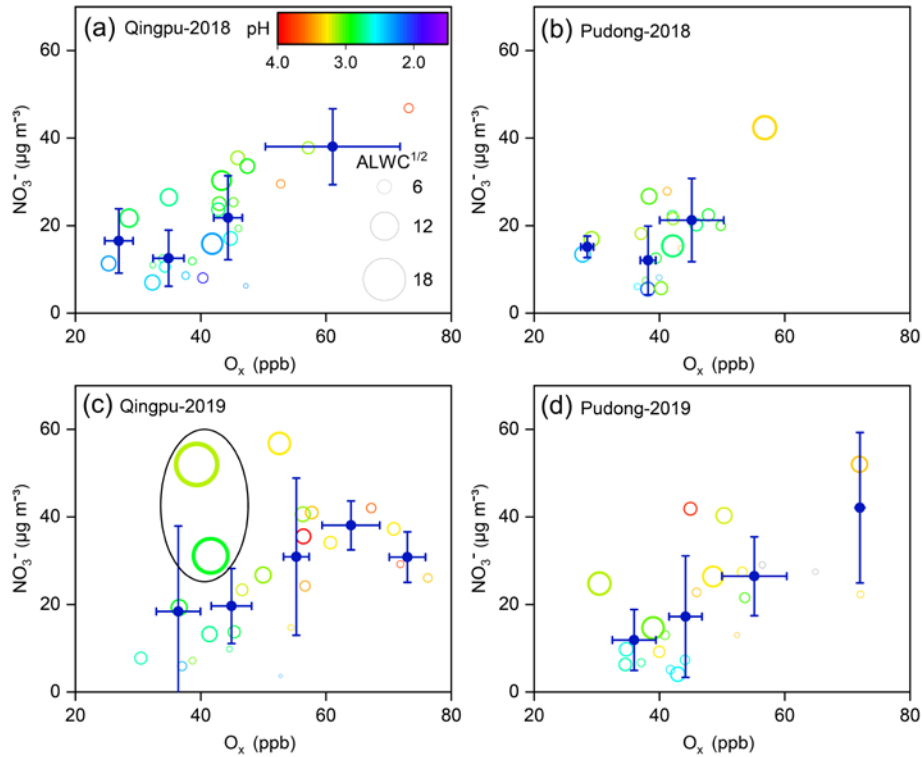
971



972

973 Figure 6 Nighttime average particulate nitrate concentration (empty circles)
 974 at (a, c) Qingpu and (b, d) Pudong sites in 2018 and 2019. The circles are colored according to aerosol
 975 pH and their size is linearly scaled with square root of ALWC. The blue filled circles represent the
 976 average of nitrate concentration within a certain $[\text{NO}_2]^2 \times [\text{O}_3]$ interval. To reduce the influences of
 977 daytime remainder on the analysis of nighttime nitrate formation, only the data with an obvious peak or
 978 increasing trend during nighttime were included in the plots.

979

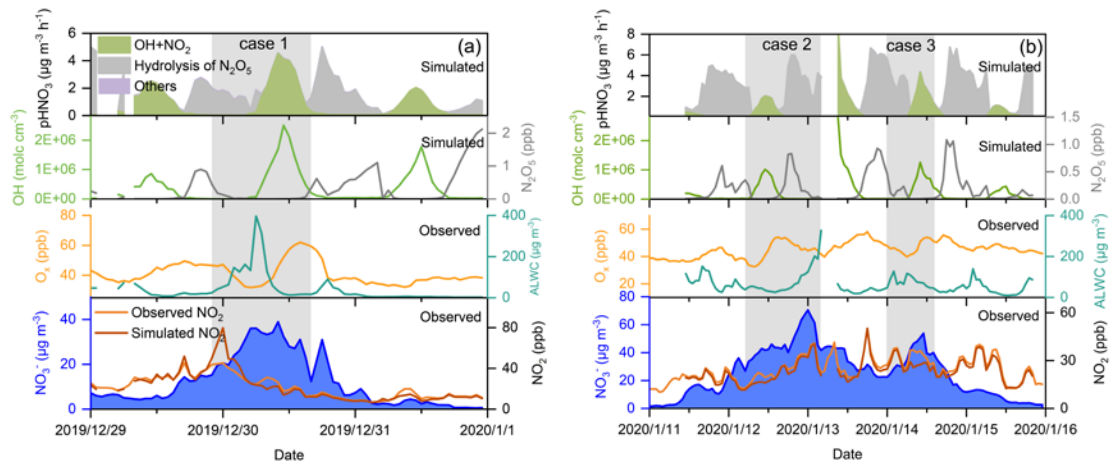


980

981 Figure 7 Daytime average particulate nitrate concentration as a function of O_x at (a, c) Qingpu and (b, d)
 982 Pudong sites in 2018 and 2019. The circles are colored according to aerosol pH and their size is linearly
 983 scaled with square root of ALWC. The blue filled circles represent the average of nitrate concentration
 984 within a certain O_x interval. The data points inside the black circle in (c) correspond to low O_x levels but
 985 high ALWC and nitrate concentrations. Only the data with an obvious peak or increasing trend during
 986 daytime were included in the plots.

987

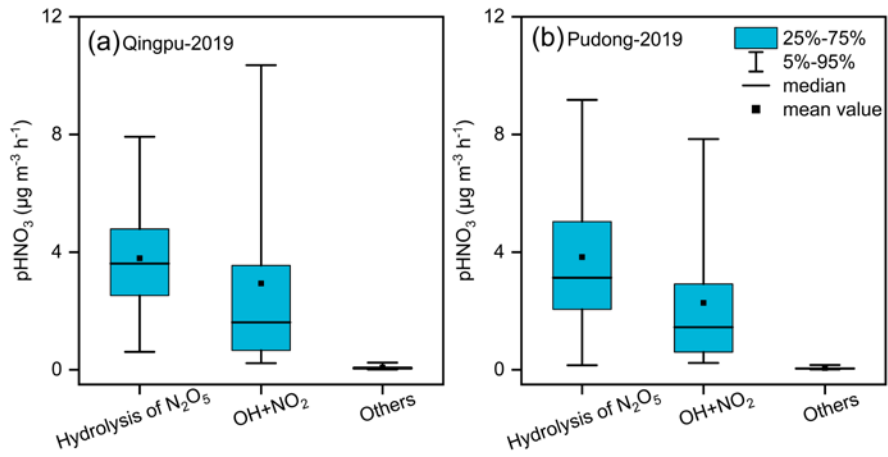
988



989

990 Figure 8 Time series of particulate nitrate, NO_2 , O_x , ALWC, OH, N_2O_5 , as well as the formation rate
 991 of HNO_3 from different processes during the two selected case during the pollution episodes at the
 992 Pudong site in 2019. The simulated data with $\text{RH} > 95\%$ were not included in the figure (see main
 993 text).

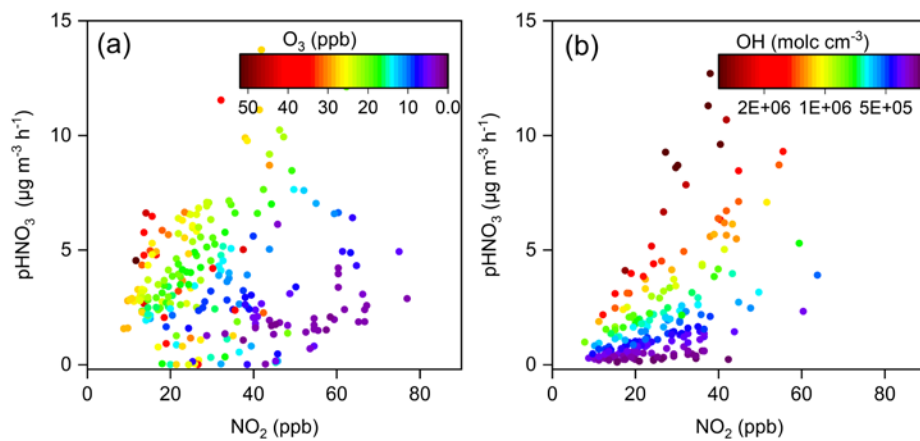
994



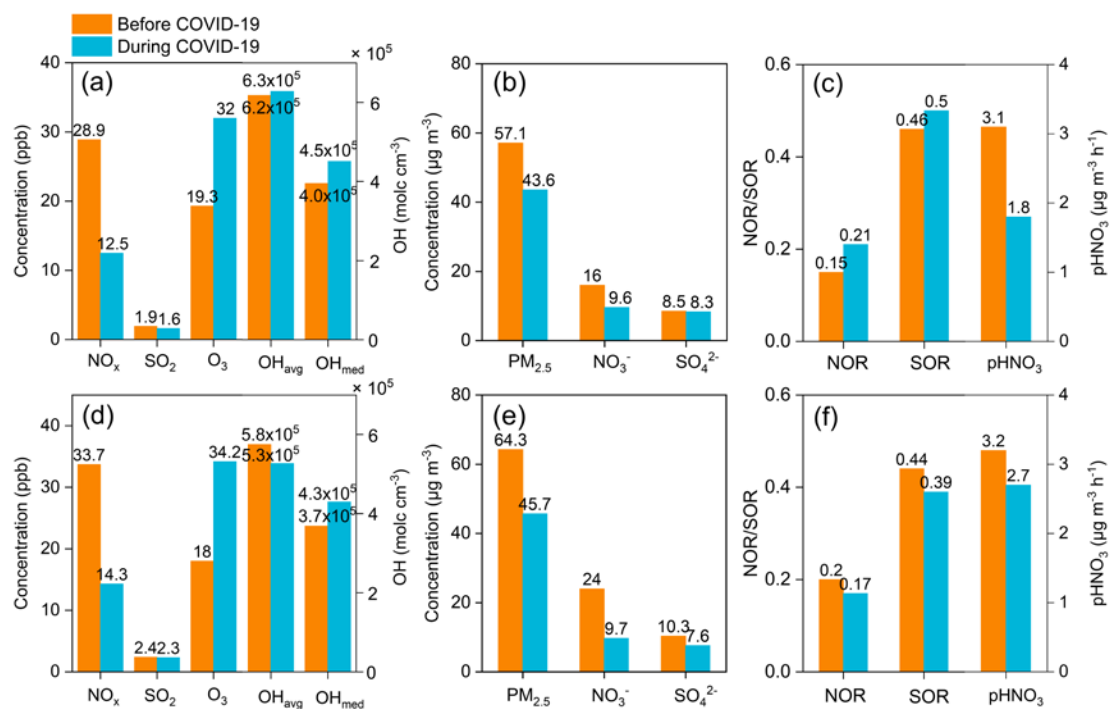
995

996 Figure 9 Simulated average formation rates of HNO_3 at (a) Qingpu and (b) Pudong sites during the
 997 haze pollution periods in 2019

998



999
 1000 Figure 10 Production rates of HNO₃ from the (a) heterogeneous and (b) gas-phase processes as a
 1001 function of NO₂ concentration at the Pudong site during the nighttime and daytime, respectively.
 1002 The circles are colored according to the O₃ concentration in (a) and OH radical concentration in (b).
 1003



1004

1005 Figure 11 Average concentrations of NO_x , SO_2 , O_3 , OH radicals, $\text{PM}_{2.5}$, nitrate, sulfate, as well as
 1006 the nitrogen and sulfur oxidation ratio (NOR and SOR) at (a-c) Pudong and (d-f) Qingpu sites before
 1007 (1-22 January, 2020) and during (23 January-12 February, 2020) the COVID-19 epidemic.